

1
2
3
4
5
6
7
8
9
10
11
12
13
14
15
16
17
18

Systems biology illuminates alternative metabolic niches in the human gut microbiome

Cecilia Noecker¹, Juan Sanchez², Jordan E. Bisanz¹⁺, Veronica Escalante¹, Margaret Alexander¹, Kai Trepka¹, Almut Heinken³, Yuanyuan Liu⁴, Dylan Dodd^{4,5}, Ines Thiele³, Brian DeFelice², and Peter J. Turnbaugh^{1,2*}

¹Department of Microbiology & Immunology, University of California, San Francisco, San Francisco, CA 94143

²Chan-Zuckerberg Biohub, San Francisco, CA 94158

³School of Medicine, National University of Ireland, Galway, Ireland

⁴Department of Pathology, Stanford University, Stanford, CA 94305

⁵Department of Microbiology & Immunology, Stanford University, Stanford, CA 94305

⁺Present address: Department of Biochemistry and Molecular Biology, Pennsylvania State University, State College, PA

*Correspondence to: Peter J. Turnbaugh, Ph.D., peter.turnbaugh@ucsf.edu

19 **SUMMARY**

20

21 **Human gut bacteria perform diverse metabolic functions with consequences for host**
22 **health. The prevalent and disease-linked Actinobacterium *Eggerthella lenta* performs**
23 **several unusual chemical transformations, but it does not metabolize sugars and its core**
24 **growth strategy remains unclear. To obtain a comprehensive view of the metabolic**
25 **network of *E. lenta*, we generated several complementary resources: defined culture**
26 **media, metabolomics profiles of strain isolates, and a curated genome-scale metabolic**
27 **reconstruction. Stable isotope-resolved metabolomics revealed that *E. lenta* uses acetate**
28 **as a key carbon source while catabolizing arginine to generate ATP, traits which could be**
29 **recapitulated *in silico* by our updated metabolic model. We compared these *in vitro***
30 **findings with metabolite shifts observed in *E. lenta*-colonized gnotobiotic mice,**
31 **identifying shared signatures across environments and highlighting catabolism of the**
32 **host signaling metabolite agmatine as an alternative energy pathway. Together, our**
33 **results elucidate a distinctive metabolic niche filled by *E. lenta* in the gut ecosystem.**

34

35 **KEYWORDS**

36 Human gut microbiome; *Eggerthella lenta*; systems biology; metabolomics; stable
37 isotope-resolved metabolomics; metabolic niche

38 **INTRODUCTION**

39 Human gut bacteria perform diverse and specialized metabolic functions with
40 consequences for host health. Yet the core metabolic strategies relied upon for growth
41 by many commensal gut microbes remain unclear, which is reflected in the large
42 number of gut taxa that remain difficult to culture (Lagkouvardos et al., 2017;
43 Tramontano et al., 2018). The growth strategies of individual gut species and strains
44 shape their ability to colonize a host and their potential chemical interactions with other
45 community members and with the host (Alexander et al., 2021; Medlock et al., 2018).
46 Efforts to describe and model the metabolism and growth of various community
47 members have included detailed biochemical studies of resource utilization by individual
48 model species such as members of the genus *Bacteroides* (Koropatkin et al., 2012) and
49 *Clostridium sporogenes* (Liu et al., 2022), as well as large-scale efforts to characterize
50 species-level metabolic activity using community multi-omic profiling (Franzosa et al.,

51 2018; Hertel et al., 2019). However, these efforts have been most fruitful for members of
52 the microbiota that are found at high abundance and with prior knowledge of well-
53 annotated metabolic pathways.

54 One key group of human gut microbes whose core metabolism remains
55 particularly unclear are those that are fully asaccharolytic; *i.e.* derive no growth benefit
56 from sugars and instead may rely on a range of more unconventional nutrients. Many of
57 these taxa are members of the family *Eggerthellaceae*, which are widely found in
58 mammalian gut microbiota (Almeida et al., 2019) but rarely found in other environments.
59 The species *Eggerthella lenta* is a notable example of this group. *E. lenta* is a gram-
60 positive facultative anaerobe found at high prevalence in human gut microbiota (Koppel
61 et al., 2018). Although *E. lenta* is commonly found in healthy individuals, it can cause
62 severe bacteremia (Gardiner et al., 2015) and is increased in abundance in the gut
63 microbiota of patients with several autoimmune diseases (Cekanaviciute et al., 2017;
64 Chen et al., 2016; Islam et al., 2021; Zhu et al., 2021).

65 *E. lenta* has distinctive metabolic properties and a capacity for many unusual
66 chemical transformations, but it remains unknown how these properties fit into its overall
67 metabolic network and evolutionary strategy. *E. lenta* strains can metabolize varied
68 mammalian and dietary substrates, including cardenolides, bile acids, plant lignans, and
69 dopamine (Bess et al., 2020; Devlin and Fischbach, 2015; Haiser et al., 2013; Koppel et
70 al., 2018; Maini Rekdal et al., 2019). However, none of these compounds except
71 dopamine have been reported to provide a growth or fitness advantage in any
72 conditions tested to date. Genome analysis of *E. lenta* has also predicted that it may be
73 able to perform autotrophic acetogenesis (Harris et al., 2018), but this prediction has not
74 been biochemically validated. *E. lenta* culture conditions typically require rich media and
75 high levels of the amino acid L-arginine. Past studies reported little to no growth of *E.*
76 *lenta* in minimal or chemically defined media formulations (Hylemon et al., 2018; Maini
77 Rekdal et al., 2020; Tramontano et al., 2018), complicating mechanistic biochemical
78 studies of its metabolism.

79 In this study, we first developed a chemically defined media that supports strong
80 growth of *E. lenta* strains and described the metabolic footprint and growth determinants
81 of *E. lenta* in this environment. We used stable isotope-resolved metabolomics (SIRM)

82 to investigate the pathways by which *E. lenta* metabolizes two key nutrients, acetate
83 and arginine. This platform allowed us to curate and interpret a genome-scale metabolic
84 model of the *E. lenta* type strain to make predictions about untested growth conditions
85 and to identify gaps in the metabolic network representing novel enzymes or pathways.
86 Extending this approach, we further documented extensive diversity in the metabolic
87 footprint of a collection of *E. lenta* strain isolates. Finally, we evaluated the relevance of
88 these findings to a host-associated context by profiling the metabolome of *E. lenta*-
89 colonized gnotobiotic mice, defining shared and divergent metabolic activities between
90 *in vitro* and *in vivo* environments. In total, we elucidate an unusual metabolic niche and
91 lay a comprehensive foundation for future mechanistic studies of *E. lenta* metabolism.

92

93 **RESULTS**

94 **Extensive metabolite footprint of *Eggerthella lenta* in chemically defined media**

95 To identify key nutrients and metabolic pathways required for growth of *E. lenta*,
96 we first developed a custom chemically defined media formulation, referred to as
97 *Eggerthella* Defined Media 1 (EDM1). We designed the initial EDM1 formulation by
98 making several modifications to a recipe previously reported to support growth of many
99 human gut bacterial isolates but not *E. lenta* (Tramontano et al., 2018). We increased
100 the quantity of L-arginine, removed sugars, and ensured the availability of all amino
101 acids and vitamins/cofactors with fragmented or missing biosynthetic pathways in the *E.*
102 *lenta* DSM 2243 genome [Virtual Metabolic Human database annotations (Noronha et
103 al., 2018), *Methods*, [Table S1](#)]. The resulting media is composed of compounds
104 typically present in the mammalian gut from microbial, host, and/or dietary sources. It
105 supported robust *E. lenta* growth at a level comparable with standard culture conditions
106 (Brain Heart Infusion media supplemented with 1% arginine; [Figure S1A-B](#)).

107 Using this platform, we sought to identify primary metabolites used and produced
108 by *E. lenta*, and the underlying core metabolic pathways active in the EDM1 condition.
109 We used untargeted metabolomics to analyze culture supernatants of the type strain *E.*
110 *lenta* DSM 2243 across 6 time points over its 50-hour growth curve in EDM1 batch
111 culture ([Figure 1A](#)). After dereplication of features from positive and negative ionization
112 modes, 4,095 features were detected, of which 636 (15.6%) were not detected in sterile

113 control media (sample mean intensity > 3x blank sample mean, **Figure 1B**). 612
114 features (14.9% of features overall) were significantly different in abundance between
115 sterile controls and supernatants at the final time point (FDR-adjusted $p < 0.1$, **Figure**
116 **1C**), of which the majority (444, 72.5%) were increased in *E. lenta* cultures. Notably, the
117 number of differentially abundant features at the final time point, both in total and among
118 those assigned an identification, is substantially higher than previously reported
119 metabolomic profiles of this species in ISP-2 and Mega media (Bisanz et al., 2020; Han
120 et al., 2021) (**Figure S1C**). This increased sensitivity was expected given our use of
121 both chemically defined culture media and untargeted metabolomics.

122 Metabolites of diverse chemical classes are modified by *E. lenta* (**Figure 1C-D**).
123 Compounds produced by *E. lenta* tended to be amino acid and nucleic acid metabolites.
124 As expected, these included ornithine and citrulline, suggesting activity from the
125 arginine deiminase pathway, which is highly expressed by *E. lenta* in the presence of
126 arginine (Haiser et al., 2013). However, other arginine-related metabolites were also
127 produced at lower levels, including N,N-dimethylarginine, N5-(1-iminoethyl)-ornithine,
128 and homocitrulline, suggesting that arginine may also be metabolized via other
129 pathways. Several other metabolites produced at lower levels appeared to be products
130 of metabolism of other amino acids in the media, including 4-methyl-2-hydroxy-
131 pentanoic acid (from leucine), indole-3-acetate and indole-3-lactic acid (from
132 tryptophan), and 3-phenyllactic acid (from phenylalanine), consistent with one previous
133 report of production of indole-containing compounds and phenyl acids by *E. lenta*
134 (Beloborodov et al., 2009). Other metabolites produced in supernatants included the
135 amino acids alanine, glutamate, glutamine, histidine, and lysine; as well as several
136 intermediates in biosynthesis of both purines and pyrimidines (inosine, orotic acid,
137 hypoxanthine, uridine, thymidine). Overall, the set of metabolites produced by *E. lenta*
138 supports its previously reported dependence on arginine catabolism, but is highly
139 multifaceted.

140 Of the 54 compounds in our EDM1 recipe, 22 were detected by untargeted
141 metabolomics but just three were depleted significantly in *E. lenta* cultures (**Figure S1D**,
142 **Figure 1D**): arginine, riboflavin, and EDTA (which is likely reduced due to complexing
143 with metal ions rather than from direct uptake or metabolism). This result suggested that

144 most compounds were included in excess, leading us to reduce the concentration of
145 several non-depleted amino acids for subsequent experiments (**Table S1**). Interestingly,
146 5 of the identified metabolite features significantly depleted by *E. lenta* were not
147 explicitly included in our defined media formulation, including guanine and five arginine
148 dipeptides (**Figure 1D**). Since these compounds were found at low intensities, were
149 annotated with high confidence, and are structurally related to intentionally included
150 compounds, we inferred that they may be trace contaminants from commercial
151 preparations of uracil and arginine (see *Methods*). Their rapid depletion indicates that
152 their presence may influence growth and metabolic activity and reinforces the value of
153 untargeted metabolomic profiling.

154 We examined the dynamics of metabolite production and depletion over the 50-
155 hour growth of *E. lenta* in batch culture. Hierarchical clustering of metabolite trajectories
156 indicated that among both produced and depleted features, some metabolites are
157 produced/depleted rapidly early in growth while others shift more dramatically later as
158 the culture approaches stationary phase (**Figure 1D, Figure S1E**). This observation
159 suggests that two or more distinct growth phases may be occurring as resources are
160 consumed from the media. Among identified metabolites, the trace guanine and
161 arginine dipeptides are first depleted from the culture in early time points while citrulline,
162 inosine, and indole-3-lactic acid are produced at relatively higher rates (**Figure 1D**). In
163 the later phase, arginine is depleted more rapidly while alanine, 4,6-
164 dihydroxypyrimidine, and various *N*-acetylated amino acid metabolites are produced.

165 To gain a better understanding of the contributions of individual nutrients to *E.*
166 *lenta* growth, we systematically tested the effect of their removal from the media on
167 growth of *E. lenta* DSM 2243 (*Methods, Table S2*). We collected growth curve data
168 from EDM1 with and without each component and fit logistic growth models to the
169 results, finding that 22 out of 41 compounds tested had a significant effect on at least
170 one of the following growth parameters (Wilcoxon rank-sum test, FDR-adjusted $p < 0.2$):
171 carrying capacity (maximum density), growth rate, time to mid-exponential, and/or area
172 under the growth curve (**Figure S2A**). The only compounds whose individual removal
173 fully prevented growth of *E. lenta* were arginine, tryptophan, riboflavin, biotin, and
174 magnesium (although it is plausible that other compounds are required in trace amounts

175 and were not fully removed by our preparation methods, particularly minerals such as
176 iron). In general, removing amino acids most commonly tended to reduce carrying
177 capacity, consistent with a role as carbon and/or energy sources, while removing
178 vitamins had more varied effects on the growth curve (**Figure S2B**).

179

180 **Acetate and arginine are key carbon and energy sources for *E. lenta***

181 Surprisingly, we found that sodium acetate contributed substantially to *E. lenta*
182 growth in EDM1 (**Figure S2A**), even though it was included at a relatively low
183 concentration (1 mM, compared to 57 mM arginine in EDM1). Since acetate is an
184 abundant and variable metabolic byproduct of diverse human gut microbes (van der
185 Hee and Wells, 2021), dependence on acetate could shape the ecological interactions
186 of *E. lenta* in the human gut microbiota. Although our untargeted LC-MS workflow was
187 not able to quantify acetate, we had observed accumulation of several *N*-acetylated
188 compounds in supernatant (**Figure 1D**), suggesting that the amount of acetate
189 incorporated into core metabolic pathways may be relatively small. However, acetate
190 provided a dose-dependent increase in carrying capacity for *E. lenta* up to a
191 concentration of at least 10 mM in EDM1 (**Figure 2A**). We therefore used a targeted
192 derivatization and LC-MS/MS method to quantify acetate levels in supernatants from
193 three strains of *E. lenta* (DSM 2243, AB8n2, and Valencia) grown in EDM1 with different
194 acetate concentrations (0, 1, or 10 mM). Acetate was depleted to approximately the limit
195 of quantification in cultures from the 1 mM acetate group, but not the 10 mM acetate
196 group, confirming that a relatively small quantity is required for the observed level of *E.*
197 *lenta* growth (**Figure S3A**). We tested the effect of replacing acetate with equimolar
198 amounts of 10 other small carbon compounds, finding that no tested alternative
199 compound provided a comparable benefit (**Figure 2B**). Based on these results, we
200 chose to further investigate *E. lenta*'s acetate utilization pathways.

201 First, we used our untargeted LC-MS metabolomics workflow to compare
202 metabolites in supernatant over time from the same three *E. lenta* strains grown in
203 EDM1 with different acetate concentrations (*E. lenta* DSM 2243 shown in **Figure 2C**,
204 AB8n2 and Valencia in **Figure S3B-C**). Using smoothing spline models, we found that
205 many produced or depleted compounds had significantly different abundance

206 trajectories across the growth phase (FDR-adjusted $p < 0.25$) depending on the presence
207 of acetate. These included pyrimidine metabolites, *N*-acetylated amino acids, amino
208 acid metabolites including indole-3-lactic acid and 2-hydroxyglutaric acid, and 423
209 unidentified metabolite features (**Figure 2C**). Of the 612 features produced by *E. lenta*,
210 53.4% had significantly different trajectories in the no acetate condition. Most
211 differentially abundant compounds were associated with cell density and produced by *E.*
212 *lenta* at higher levels when grown with higher acetate concentrations, reinforcing the
213 general loss of biomass production in the absence of acetate.

214 To identify the specific pathways by which acetate is metabolized by *E. lenta*, we
215 next profiled metabolites in the supernatant across time during growth of the same three
216 strain isolates of *E. lenta* with $^{13}\text{C}_2$ acetate provided as a stable isotope-labeled
217 substrate (DSM 2243 in **Figures 2D-F**, 2 additional strains in **Figure S4**). We detected
218 the incorporation of ^{13}C labeled atoms in 52 features in *E. lenta* supernatants at the final
219 time point, of which 24 were previously identified as responsive to acetate
220 concentrations (*Methods*, **Figures 2D, S4**). Acetate was incorporated into diverse
221 products across metabolite classes, but was found at the highest enrichment levels in
222 nucleotide and carbohydrate metabolites (**Data S1**).

223 Because many core metabolites are not produced in excess or secreted during
224 growth, we also analyzed intracellular metabolites from extracts collected at a single
225 time point in the late-exponential growth phase. Labeled intracellular compounds
226 included glutamate, glutamine, sugars, nucleotide metabolites, and UDP-*N*-acetyl-
227 glucosamine, a primary component of peptidoglycan (**Figure 2E**), as well as seven
228 labeled compounds of unknown identity. The signal from carbohydrate-related
229 compounds including glucose-6-phosphate and UDP-*N*-acetyl-glucosamine was almost
230 exclusively from labeled isotopologues (97.5% in 1 mM acetate and 100% in 10 mM
231 acetate), indicating that synthesis of these compounds using acetate may be more
232 efficient than any alternative non-acetate-dependent pathways available to *E. lenta* in
233 the EDM1 condition.

234 Acetate-derived extracellular and intracellular metabolites were consistent across
235 the two additional strains of *E. lenta*. While the overall rate of acetate incorporation
236 differed between the three strains, the set of extracellular and intracellular labeled

237 compounds was fully consistent. Isotopic enrichment for two additional extracellular
238 metabolites (malonic acid and 3-hydroxy-myristic acid) was identified in both of these
239 strains as well as four additional intracellular metabolites in one or both strains (all of
240 unknown identity), confirming that acetate is incorporated by *E. lenta* into varied
241 biosynthetic pathways (**Figure S4**).

242 Based on these results and metabolic gene annotations of the *E. lenta* DSM
243 2243 genome, we hypothesized that *E. lenta* converts acetate to acetyl-CoA via acetate
244 kinase (ELEN_RS08645) and phosphate acetyltransferase (ELEN_RS08640). Acetyl-
245 CoA could then be used as a carbon source via two routes: conversion to glutamate by
246 a partial citric acid cycle, and synthesis of pyruvate by the enzyme pyruvate-ferredoxin
247 oxidoreductase (PFOR, ELEN_RS10770) (**Figure 2F**). This hypothesis is consistent
248 with the organization of the *E. lenta* DSM 2243 genome, as two of the three enzymes
249 required for conversion of acetyl-CoA to glutamate are co-located (aconitate hydratase
250 and isocitrate dehydrogenase, ELEN_RS11710, ELEN_RS11715). Genes for another
251 partial component of the citric acid cycle—fumarate hydratase and malate
252 dehydrogenase—are co-located in another region of the genome (ELEN_RS056[70-
253 90]), suggesting they may act in a separate functional role. Taken together, these data
254 suggest that *E. lenta* uses acetate as a key carbon source for synthesis of biomass
255 components, in tandem with ATP generation from arginine catabolism, anaerobic
256 respiration, and/or other unknown pathways.

257 However, we inferred that acetate is likely not the sole carbon source used by *E.*
258 *lenta* in EDM1, given the relatively low concentration required for growth promotion and
259 the abundance of unlabeled isotopologues detected for many produced compounds
260 (**Data S1**). We wondered whether arginine or ornithine may also be substrates for
261 synthesis of biomass components, or if arginine is exclusively catabolized to ornithine
262 for ATP production, as suggested by one previous study in rich media (Sperry and
263 Wilkins, 1976). We first confirmed that citrulline, but not ornithine, can replace arginine
264 with nearly equivalent growth in EDM1, replicating a previous result in rich media
265 [(Haiser et al., 2013), **Figure S5A**]. We then analyzed intracellular and extracellular
266 metabolites from *E. lenta* DSM 2243 growing in EDM1, this time with $^{13}\text{C}_6$ L-arginine as
267 a stable isotope-labeled substrate. We found by far the largest composition of ^{13}C

268 enriched isotopologues in ornithine, citrulline, and other closely related compounds
269 (**Figure S5B-E**), indicating that arginine is predominately processed by the arginine
270 deiminase pathway. However, we observed M+1 enrichment (i.e. incorporation of a
271 single ^{13}C carbon atom from arginine) in produced glutamine, orotic acid, and
272 pyrimidines, among others (**Figure S5C-D**), suggesting biosynthesis from the
273 carbamoyl phosphate intermediate. Labeled M+5 isotopologues of proline and
274 prolinamide also appeared at low levels at later time points, likely indicating a slower
275 flux producing these compounds from accumulated ornithine (**Figure S5D-E**). Yet in
276 total, only 29/324 features were detected with ^{13}C enrichment for five or more carbon
277 atoms in intracellular extracts, and most appeared closely related to arginine, citrulline,
278 and ornithine (**Data S1**). These results confirm that arginine is primarily an energy
279 source and not a major biosynthetic precursor for *E. lenta* (**Figure S5F**).

280

281 **A genome-scale metabolic model of the *E. lenta* type strain recapitulates growth,** 282 **metabolite, and gene expression phenotypes**

283 COstraint-based Reconstruction and Analysis (COBRA) is a set of
284 computational tools that has been applied to interpret -omics data and optimize
285 metabolic activities for various microbes of importance in basic science, metabolic
286 engineering, and medicine (Gu et al., 2019; Monk et al., 2017; Zhang et al., 2017). It
287 has been proposed as a promising strategy to predict phenotypes and design
288 modifications to complex host-associated microbial communities by synthesizing
289 information about the physiology of individual members and the available nutrients into
290 a rational framework (Chiu et al., 2014; Diener et al., 2020; Hertel et al., 2019).
291 However, the value of such a framework is dependent on its ability to accurately
292 describe the contributions of metabolically active community members. The
293 reconstructions currently available for many anaerobic microbes have only been curated
294 to a limited degree and remain minimally validated. Therefore, we used our *in vitro*
295 platform to curate and analyze a genome-scale metabolic network model of *E. lenta*
296 DSM 2243 growth in EDM1 and assessed the degree to which this model can explain *E.*
297 *lenta* metabolic phenotypes across conditions.

298 We obtained a genome-scale metabolic reconstruction from the AGORA
299 database version 2.0.0 (Heinken et al., 2020), which we term iEL2243_2. Initial testing
300 indicated that the model was incapable of biomass production in EDM1 media, so we
301 performed additional curation of model reactions and transporters (**Table S3**). We
302 curated the reconstruction based on genome annotations from multiple sources (Henry
303 et al., 2010; Pascal Andreu et al., 2021; Price et al., 2022) and added transporters for
304 strongly depleted and produced compounds that were identified with high confidence in
305 our metabolomics data. Throughout this process, we compared model results with
306 experimentally observed growth in chemically defined media conditions, using these
307 results to inform the curation process and add missing reactions where supported by
308 experimental data. We simulated metabolic fluxes in different conditions by converting
309 media concentrations into estimated maximum nutrient uptake rates for each
310 compound. While these models are typically validated by comparison with gene
311 essentiality data (Thiele and Palsson, 2010), the tools to generate such data are not yet
312 available for *E. lenta*. We instead evaluated whether the model was consistent with
313 observed metabolite utilization and production and with gene expression during
314 exponential growth in EDM1, and whether predicted essential genes were conserved
315 across strain genomes.

316 This process resulted in a model with 1,244 reactions linked to 727 gene
317 annotations and 1,218 metabolites (**Figure 3A**). The largest number of reactions were
318 in the subsystems of fatty acid synthesis, extracellular transport, and
319 glycerophospholipid biosynthesis (**Figure 3B**). Flux balance analysis of the final model
320 estimated the maximum growth rate of *E. lenta* DSM 2243 in EDM1 to be 0.96 hr^{-1} ,
321 higher than experimental values (median 0.32 hr^{-1} , **Figure S2B**). The existence of a
322 difference between these values is not surprising given that organisms do not
323 necessarily grow at their theoretical maximum growth rate, and growth constraints may
324 exist that are not encoded in the metabolic network model (Thiele and Palsson, 2010).
325 However, the relatively large discrepancy indicates that additional modifications to the
326 biomass equation may further improve the model.

327 The initial model with nonzero growth in EDM1 did not recapitulate the
328 experimentally observed dependencies on either arginine or acetate (**Figure 3C**). We

329 noticed that this lack of dependency was linked to the inclusion of Wood-Ljungdahl
330 acetogenesis reactions in the model, previously suggested to be present in *E. lenta*
331 (Harris et al., 2018; Hylemon et al., 2018). The presence of these reactions allowed the
332 model to draw on an effectively unlimited source of acetyl-CoA from CO₂ and H₂.
333 Regardless of whether the previous annotation of this pathway (which has not been
334 biochemically validated) is correct, reductive acetogenesis may not be
335 thermodynamically favorable during *in vitro* growth in our anaerobic chamber, where the
336 H₂ concentration is ≤ 5% (Smith et al., 2020). Blocking model flux through the carbon
337 monoxide dehydrogenase reaction of this pathway increased growth dependency on
338 uptake of both arginine and acetate, reflecting our experimental observations (**Figure**
339 **3C**). The model also found no growth benefit from pyruvate, citrate, and other fatty acids
340 based on a lack of annotated transporters for these compounds, consistent with
341 experimental results.

342 In another key curation step, required to enable biomass production by the model
343 in EDM1, we noticed that *E. lenta* lacks an annotated gene for the enzyme enoyl-acyl
344 protein carrier reductase, which performs the elongation in the typical type 2 fatty acid
345 synthesis pathway used in bacteria. Because fatty acid biosynthesis is essential and
346 previous studies have noted a high level of diversity in this essential step among
347 bacterial genomes (Massengo-Tiassé and Cronan, 2009), we preserved this step in the
348 model without any current gene annotation. This gap may indicate a novel enzyme
349 family performing this conversion (**Table S3**).

350 We applied the iEL2243_2 model to predict growth phenotypes across our leave-
351 one-out chemically defined media conditions, finding that these were generally
352 consistent with some remaining notable exceptions (**Figure 3D**, overall Matthews
353 correlation of 0.35, Fisher exact test odds ratio=9.1, *p*=0.06). Amino acid dependencies
354 matched well between the model and experimental data, with the exception of cysteine,
355 which likely provides a benefit as a reducing agent that is not accounted for by the
356 model (Strobel, 2009). Vitamin dependencies were also generally consistent, with the
357 notable exception of folate, which had no effect on growth despite the lack of several
358 genes for reactions in the canonical folate biosynthesis pathway and the absence of a
359 known dihydrofolate reductase enzyme (Rodionov et al., 2019). The phenomenon of

360 presumed-essential but absent folate genes in bacterial genomes has been recognized
361 previously (de Crécy-Lagard et al., 2007; Levin et al., 2004; Rodionov et al., 2019),
362 suggesting the possible existence of undiscovered alternative enzymes. Notably, growth
363 was negatively affected by the removal of the folate precursor *p*-aminobenzoate (**Figure**
364 **S2A**). Most of the remaining discrepancies between the model and the growth data are
365 in conditions in which metal ions were removed, which were expected to be required by
366 the model (Cu^{2+} , Ca^{2+}) but were not essential based on our experiments (**Figure 3E**).
367 However, these likely reflect difficulties in fully removing trace minerals in our
368 experiment rather than errors in the model reconstruction.

369 While we curated the model based on growth data, we did not incorporate our
370 metabolomics data except to add transporters for highly differentially abundant
371 metabolites. Even so, we found that there was a high correspondence between
372 observed metabolite shifts and the possible uptake and secretion fluxes inferred by flux
373 variability analysis (FVA) of the model. FVA identifies the range of fluxes for each
374 reaction that are compatible with near-maximum growth. All 37 identified metabolites
375 present in both the model and our metabolomics data displayed experimental shifts in
376 abundance qualitatively compatible with inferred flux ranges (**Figure 3F**), providing
377 additional support for model quality.

378 We further compared the iEL2243_2 inferred flux profile with RNA-Seq data from
379 *E. lenta* growing in this condition, which was not used for model curation (*Methods*).
380 71.9% of genes linked to active reactions were in the top half of metabolic genes by
381 expression level in the EDM1 condition (> 109 transcripts per million), and 91.9% were
382 in the top 75%. Expression level and absolute flux magnitude were highly correlated
383 across all genes linked to metabolic reactions (Spearman $\rho=0.34$, $p<2.2\times 10^{-16}$, **Figure**
384 **3G**). While we would not expect a perfect correlation between expression and metabolic
385 flux, correspondence between the two provides support that our model has correctly
386 identified pathways with high activity.

387 Having established consistency with experimental data, we next examined
388 overall reaction fluxes and key pathways in the final model. We found that fewer than
389 half of reactions were predicted to be active in EDM1 by parsimonious flux balance
390 analysis (pFBA, **Figure 3A**). In the pFBA solution, acetate is incorporated into a partial

391 reductive citric acid cycle via pyruvate formate oxidoreductase (PFOR), which then
392 feeds lipid and carbohydrate biosynthesis pathways, consistent with our SIRM results
393 and with our RNA-Seq data, where PFOR was one of the most highly expressed genes.
394 The vast majority (99.6%) of arginine uptake flux was directed to ATP generation, and
395 58.4% of ATP generation was sourced from the arginine deiminase pathway (which
396 contains the 1st, 3rd, 4th, and 5th most highly expressed protein-coding genes in our
397 RNA-Seq data, [Table S4](#)). The remainder of ATP generation in the pFBA solution was
398 attributed to anaerobic respiration via an ATP synthase reaction, although the specific
399 electron transport chain substrates were not clear. However, consistent with this
400 hypothesis, genes linked to respiration were expressed at moderate levels, including
401 ATP synthase subunits and an Rnf electron transport complex, and *E. lenta* is known to
402 have a large number of poorly characterized enzymes potentially involved in electron
403 transfer (Maini Rekdal et al., 2020; Ravcheev and Thiele, 2014). The model also
404 identified the regeneration of NADP⁺ via transaminase reactions (using mainly pyruvate
405 and/or branched chain amino acids) and glutamate dehydrogenase as a key high-flux
406 pathway.

407 Finally, we applied the model to predict the effects of knocking out individual
408 reactions on growth of *E. lenta*. 15.3% of all reactions in iEL2243_2 were predicted to
409 be essential in any condition and 19.4% to be essential in EDM1. These reactions
410 tended to be involved in lipid metabolism, cell wall biosynthesis, and transport of
411 essential metabolites ([Figure S6A](#)). Genes linked to reactions whose removal reduced
412 growth to < 70% of wild type levels were found in a greater number of *E. lenta* strain
413 genomes than other genes (Wilcoxon rank-sum test, $p=0.001$, [Figure S6B](#)) and were
414 more likely to be part of the core genome (found in all strains; Fisher exact test odds
415 ratio = 1.74, $p=0.0002$). Overall, while significant manual curation was required for the
416 model to recapitulate realistic growth in EDM1, our updated model is able to predict and
417 interpret many aspects of *E. lenta* growth and metabolic activity across conditions.

418

419 **The strain-variable *E. lenta* metabolome is enriched for nucleotides and cell wall**
420 **metabolites and can be linked to genome variation**

421 Our initial efforts to characterize *E. lenta* core metabolism focused mainly on the
422 type strain. However, *E. lenta* has an open pan-genome and established variability in
423 secondary and xenobiotic metabolism (Bisanz et al., 2020). We therefore evaluated the
424 extent to which the metabolic profile of this species is conserved across a larger number
425 of strain isolates. We used untargeted metabolomics to profile stationary phase
426 supernatants of 30 strains grown in EDM1 (**Figure S7A-B**) and used linear models to
427 identify features with significant strain-associated differences in abundance. Over half of
428 the features produced by the UCSF DSM 2243 type strain (52.8%) were variable across
429 strains of *E. lenta* (**Figure 4A**), and 1,097 features produced by at least two other
430 strains were not produced by the type strain. Divergence in metabolite profiles between
431 strains was not associated with phylogenetic divergence based on an alignment of core
432 genes (Procrustes analysis, $p=0.31$, **Figure 4B**), consistent with previous findings from
433 untargeted metabolomics profiling of these strains in rich media with a different
434 metabolomics platform (Bisanz et al., 2020). Overall metabolite profiles were
435 moderately associated with presence/absence patterns of variable gene families
436 between strains ($p=0.03$, **Figure 4B**), indicating that the presence or absence of
437 biosynthetic genes and pathways only partly explains variation in the metabolome and
438 that other factors like gene regulation and enzymatic activity may also play a substantial
439 role.

440 While strain-variable metabolites were quite diverse, they were enriched for
441 certain chemical classes. 92.0% of strain-variable metabolites had no identity
442 information, a similar ratio to the total number of metabolite features (91.8% of features
443 in the whole dataset). Among other features, organic acids (which included many amino
444 acid metabolites) were the least likely to be strain-variably produced. In contrast,
445 organic oxygen compounds (which included several features identified as sugars) and
446 nucleotide metabolites were more likely to be strain-variably produced, and organic
447 heterocyclic compounds and benzenoids were enriched for strain-variable depletion
448 (**Figure 4C**). The share of strains producing any individual feature varied widely (**Figure**

449 **4C**), although the largest number of features (76.8%) were produced by either only a
450 few (<4) strains or nearly all (>27) strains (**Figure S7C**).

451 Given the large share of unidentified metabolites in our dataset, we evaluated
452 whether linking strain-variable metabolites with strain-variable genes could inform
453 metabolite annotations. We performed an association analysis between metabolite
454 feature abundances and the presence of specific accessory gene families, applying a
455 method developed for previous analysis of this *E. lenta* strain collection (Bisanz et al.,
456 2020). A full 39.0% of metabolite features were significantly associated with the
457 presence of one or more variable gene families (FDR-adjusted $p < 10^{-4}$). Using stricter
458 filtering criteria for significance, effect size, and separability, 84 metabolite features
459 (1.3%), of which 80 had no annotation, were linked with the presence of variable genes
460 (**Table S5, Methods**). Gene families linked to these features were enriched for KEGG
461 annotations in sulfur metabolism ($q = 0.00017$), ABC transporters ($q = 0.02$), porphyrin
462 metabolism ($q = 0.03$), and biosynthesis of nucleotide sugars ($q = 0.049$), consistent
463 with the profile of identified variable metabolites.

464 As a case study, we further examined two of the top hits from this analysis, two
465 closely related but unidentified metabolite features highly associated with the presence
466 of two adjacent gene families (**Figure 4D**). These gene families were annotated by
467 Prokka (Seemann, 2014) as ribulose-5-phosphate reductase 1 (*tarI*) and a ribitol-5-
468 phosphate cytidyltransferase (*tarJ*), which are essential enzymes in the biosynthesis
469 of CDP-ribitol teichoic acid. Teichoic acids are an abundant component of the cell wall
470 of gram-positive bacteria that can take multiple forms and can be synthesized with
471 either CDP-glycerol or CDP-ribitol subunits (Brown et al., 2013; Percy and Gründling,
472 2014; Weidenmaier and Peschel, 2008). Interestingly, the m/z value and MS2 spectrum
473 of the linked features were consistent with an annotation as the two dominant [M+Cl]-
474 naturally occurring isotope adducts of a 5-carbon sugar alcohol - *i.e.* potentially ribitol,
475 xylitol, or a related compound.

476 Further examination of the *tar/tag* biosynthetic gene cluster in which these genes
477 are located revealed extensive strain diversity, with 10 different gene arrangements
478 across the 30 isolates (**Figure S7D**), suggesting recent positive selection possibly as a
479 form of phage defense (Buttimer et al., 2022; Soto-Perez et al., 2019) or host immune

480 interaction (van Dalen et al., 2020). Most genomes have one or more genes with
481 homology to *E. coli* *arnC* genes in this region, indicating that the products may be
482 lipoteichoic acids anchored to the cell membrane rather than wall teichoic acids (Percy
483 and Gründling, 2014). Among *E. lenta* genomes without *tarI* and *tarJ*, all except the type
484 strain have a *tagD* gene in the same region instead, which catalyzes the synthesis of
485 CDP-glycerol subunits instead of CDP-ribitol (**Figure S7D**) and would be consistent with
486 the absence of extracellular ribitol in those strains. Two other metabolite features were
487 associated with the presence of other members of this gene cluster, possibly indicative
488 of other strain-variable cell wall components (**Table S5**). This example illustrates that
489 comparative multi-omics can be a powerful strategy to identify and begin to decipher the
490 functional consequences of strain variation, even when metabolite identities are not
491 confirmed.

492 In addition to the unbiased association analysis above, we also assessed
493 whether strain variation in metabolites of known identity could be predicted based on
494 relevant gene annotations. We created genome-scale metabolic reconstructions of a
495 subset of strains included in this experiment ($n = 24$, using the DEMETER pipeline),
496 curated them using a limited version of the process applied to the type strain (*Methods*),
497 and again predicted growth and reaction fluxes in EDM1 and in leave-one-out media
498 conditions using flux balance analysis. Across the metabolic networks of *E. lenta*
499 strains, most reactions were conserved, including arginine metabolism and central
500 carbon metabolism (**Table S6**). Tryptophan and riboflavin auxotrophies were also
501 predicted to be conserved across strains. Variable reactions tended to be in the
502 subsystems of transport, fatty acid biosynthesis, cell wall biosynthesis, and nucleotide
503 interconversion (**Figure S7E**). Consistent with the central role of arginine metabolism,
504 ornithine and citrulline levels in our metabolomics dataset were very consistent across
505 strains. Ornithine was among the least variable metabolite features (**Figure 4D**), and
506 one of the most correlated with biomass (as estimated by optical density, Spearman
507 $\rho=0.36$, FDR-adjusted $p=0.1$).

508 While the predicted effects of most compounds on growth were similar or
509 identical across strains (**Figure S7F**), we noticed a clear difference in pantothenic acid
510 dependence, as a subset of strains were predicted to be unable to grow in its absence.

511 These strains lack the final enzyme in the biosynthesis pathway for pantothenic acid,
512 which is itself a precursor of coenzyme A. Pantothenic acid was depleted to varying
513 degrees in our metabolomics data, reaching the lowest levels in strains that lack
514 pantothenic acid synthase (**Figure 4D**). Notably, M+2 isotopologues of pantothenic acid
515 were also detected in supernatants from the acetate SIRM experiment, corroborating
516 that at least three *E. lenta* strains synthesize this vitamin *de novo* (**Data S1, Figure**
517 **S4B, Figure 2F**). We tested growth of pantothenate synthase-lacking strains in
518 comparison with a subset of genetically similar strains in EDM1 with or without
519 pantothenic acid, confirming that strains without this gene family had a greatly reduced
520 carrying capacity in the absence of pantothenic acid (**Figure 4E**) and highlighting the
521 ability of curated genome-scale models to predict phenotypic differences. Overall, our
522 analysis of strain variation in metabolite profiles is consistent with a model in which *E.*
523 *lenta*'s distinctive central carbon and energy metabolism is a core species trait, while
524 more peripheral biosynthetic pathways including synthesis of cofactors and cell surface
525 components can vary freely to adapt to specific microenvironments (Monk et al., 2013).

526

527 **Comparison of *E. lenta*'s metabolic profile *in vitro* and *in vivo* identifies shared** 528 **signatures and usage of a novel nutrient**

529 Having characterized the metabolic profile of the *E. lenta* species in a simplified
530 *in vitro* environment, we next asked how these findings compare with its metabolic
531 activity in a host, and whether our *in vitro* platform could help identify metabolic
532 processes performed by *E. lenta* within the gastrointestinal tract. We monocolonized
533 germ-free (GF) mice with one of three strains of *E. lenta* by oral gavage, collected
534 serum and intestinal contents after two weeks of colonization, and profiled metabolites
535 using the same LC-MS/MS untargeted metabolomics workflow as above. We identified
536 features that were significantly differentially abundant in *E. lenta*-colonized mice vs. their
537 GF counterparts using linear mixed models and compared these features with our *in*
538 *vitro* metabolomics datasets, identifying metabolites consistently shifted by the presence
539 of *E. lenta* across environments. After data processing, quality filtering and
540 dereplication, we obtained a dataset of 19,714 metabolite features from intestinal
541 samples. Of these, 16.7% were significantly differentially abundant (FDR-adjusted

542 $p < 0.2$) in response to colonization with at least one strain in at least one segment of the
543 intestinal tract, indicating a substantial metabolic impact of *E. lenta* on the intestinal
544 environment (**Figure S8A**). Interestingly, despite previous data showing colonization of
545 *E. lenta* DSM 2243 at similar levels from the ileum to the colon in GF mice (Bisanz et
546 al., 2020), only 1.6% of features were significantly shifted in the ileum, compared with
547 11.5% in colon and 8.1% in the cecum. Additionally, only 21 features (0.41%) were
548 differentially abundant in serum in response to any of the three strains. Overall
549 separability of metabolite profiles between germ-free and colonized was also highest in
550 the cecum and colon (**Figure 5A**). These results indicate that *E. lenta*'s strongest
551 metabolic effects are restricted to the lower intestinal tract.

552 We assessed the extent to which metabolite features produced by *E. lenta* in cell
553 culture are detectably shifted by the presence of *E. lenta* in mice. To do so, we
554 integrated our processed metabolomics datasets by linking metabolite features across
555 datasets with highly similar m/z , RT, and MS2 spectra (see *Methods*). Based on this
556 analysis, 37.2% of identified metabolite features in intestinal contents and 12.2% of
557 features overall were also detected *in vitro* (**Figure S8B**). We compared the estimated
558 \log_2 fold change of each linked feature *in vitro* with the corresponding shifts *in vivo* (full
559 set in **Data S2**; **Figure 5B** shows the comparison with the strain collection dataset in
560 **Figure 4**, **Figure S8C** shows a comparison with the dataset in **Figure 1**). 202 features
561 significantly increased by the presence of *E. lenta* DSM 2243 in cecal contents were
562 also increased in one of our EDM1 *in vitro* datasets, providing support that they are
563 directly produced by *E. lenta in vivo*. These features represented 78.9% of the set that
564 could be linked across datasets and 20.9% of the full set of *E. lenta* DSM 2243-
565 increased features in cecal contents. Only 18 metabolites depleted in cecal contents
566 were similarly depleted *in vitro*, but only three of the other 405 depleted features were
567 detected *in vitro* at all, indicating that *E. lenta* likely uses a much richer set of nutrients *in*
568 *vivo* than those available in EDM1. Overlapping produced and depleted metabolites
569 were found in greater abundance in the cecum and colon than the ileum and serum
570 (**Figure 5B**), again suggesting a greater metabolic footprint of *E. lenta* in the lower
571 gastrointestinal tract relative to other sites.

572 Ornithine was among the most increased features across sampling sites and
573 strains, consistent with our *in vitro* data (**Figure 6A**, **Figure S9A**). Other consistently
574 increased features included 5-methyluridine, citrulline, glutamine, and lysine (**Data S2**).
575 Interestingly, arginine was only significantly reduced by colonization with one of the
576 three *E. lenta* strains in this experiment (**Figure S9B**). However, most other
577 proteinogenic amino acids were increased in abundance in intestinal contents in
578 colonized mice compared with GF (**Figure S9C**), likely due to differences in host
579 activity, so the absence of an increase in arginine may be consistent with arginine
580 usage by *E. lenta*.

581 Given these results, we evaluated what other substrates may be used as carbon
582 or energy sources by *E. lenta in vivo*. The metabolites most strongly depleted by the
583 presence of *E. lenta* DSM 2243 in the intestinal tract included several fatty acids
584 conjugated with carnitine as well as multiple other nitrogen-containing metabolites:
585 saccharopine and agmatine (**Figure 6A**). We chose to investigate agmatine usage
586 further for several reasons: its chemical similarity to arginine, the presence of known
587 agmatine utilization genes in the *E. lenta* type strain genome, evidence of a consistent
588 decrease across all three strain colonization groups (**Figure S9A**), and its multiple roles
589 as a microbial metabolite and a host metabolite involved in regulation of cell division
590 and neural signaling (Piletz et al., 2013). The *E. lenta* DSM 2243 genome contains two
591 complete and two partial operons encoding genes for the agmatine deiminase pathway.
592 This pathway operates analogously to the arginine deiminase pathway, with ATP
593 production via carbamate kinase as the final step (**Figure 6B**). Despite this similarity,
594 the agmatine deiminase enzyme family is highly structurally distinct from arginine
595 deiminase (Llácer et al., 2007). Presence of this pathway is conserved across strains,
596 as other *E. lenta* genomes contain anywhere between one and four copies of the key
597 genes for agmatine deiminase and putrescine carbamoyltransferase (KEGG, **Table**
598 **S7A**). Additionally, a transcriptional regulator found adjacent to this operon in some
599 strains was previously associated with *E. lenta* competitive fitness *in vivo* (Bisanz et al.,
600 2020).

601 Based on these observations, we predicted that *E. lenta* may be able to grow in
602 the absence of arginine if it is supplied with agmatine as an alternative energy source. A

603 flux balance analysis simulation of *E. lenta* in agmatine-based EDM1 predicted a
604 somewhat reduced maximum growth rate (0.54 vs. 0.96 hr⁻¹) in this condition, with
605 arginine synthesized for protein via its annotated biosynthetic pathway from glutamate.
606 Indeed, we found that replacing arginine with agmatine introduced a growth lag but
607 resulted in a slightly higher final carrying capacity than the equivalent amount of
608 arginine (**Figure 6C**). We additionally investigated agmatine-responsive genes using
609 RNA-Seq. We grew *E. lenta* DSM 2243 in a formulation of EDM1 with 70% of the
610 standard levels of arginine and acetate, treated cultures with either concentrated
611 agmatine solution or water, and extracted RNA for sequencing. The genes most
612 strongly induced by treatment with agmatine were two copies of putrescine
613 carbamoyltransferase, one copy of agmatine deiminase, and a transporter in the same
614 operon (**Figure 6D** and **Table S7B**). Genes in the second complete agmatine
615 deiminase operon (ELEN_RS110[05-15]) were not differentially expressed, suggesting
616 that the annotation of this second operon may be incorrect and/or may be involved in
617 metabolism of a related compound. Interestingly, the most strongly downregulated
618 genes were two transport-related genes adjacent to the energy-conserving
619 hydrogenase (Ech) complex (ELEN_RS078[45-50]), one of which has structural
620 homology to the arginine-ornithine antiporter found in the arginine deiminase operon
621 (ELEN_RS09745, 27.6% identity). These results indicate that *E. lenta* can generate
622 ATP from agmatine as a distinct alternative to arginine both *in vitro* and *in vivo* and has
623 extensive genetic machinery to efficiently and specifically use each of these
624 compounds.

625

626 **DISCUSSION**

627 In this study, we used custom growth media and untargeted metabolomics to
628 profile the metabolism of a poorly understood gut microbe at a systems level. Although
629 *E. lenta* is found at > 50% prevalence in gut microbiota of North American adults
630 (Koppel et al., 2018) and linked to acute and chronic disease (Alexander et al., 2021),
631 very little is known about its core metabolic properties. We documented an unusual set
632 of carbon sources, nutrient dependencies, and secreted metabolites, and incorporated
633 these into a genome-scale metabolic model that accurately recapitulated pathway

634 activity and response to new environments. We further identified core and strain-
635 variable properties across a large collection of strain isolates. Finally, we evaluated the
636 extent to which these *in vitro* and *in silico* findings can inform our understanding of the
637 host-associated *in vivo* metabolic activity of this organism. This broad strategy
638 uncovered several specific new findings on *E. lenta*'s role in the gut microbial
639 ecosystem and its potential effects on human hosts.

640 We first analyzed *E. lenta*'s metabolic footprint in a sensitive chemically defined
641 environment using untargeted metabolomics. The extent and variety of compounds
642 produced by *E. lenta* across multiple growth phases is consistent with previous
643 experimental and theoretical work on “costless” metabolite secretions by diverse
644 microbes (Chodkowski and Shade, 2020; Dunphy et al., 2021; Pacheco et al., 2019). In
645 particular, many nucleotides and nucleic acid intermediates are synthesized by *E. lenta*
646 and secreted without any apparent cost to growth. Secretion of these broadly useful
647 metabolites may contribute to a previously observed outsized impact of *E. lenta* on the
648 composition of synthetic communities (Venturelli et al., 2018). Interestingly, several
649 small molecules produced by *E. lenta* in EDM1 and in mice are known to impact host
650 immune signaling, including indole-3-acetate (Roager and Licht, 2018) and inosine (Li et
651 al., 2021; Mager et al., 2020). Notably, the relative level of production of these
652 metabolites and others varied widely across *E. lenta* strain isolates. Teichoic acids,
653 identified here as another strain-variable feature, are also key targets of host innate
654 immunity, with differential responses depending on their composition (van Dalen et al.,
655 2020). While much focus has been deservedly paid to individual specialized
656 immunomodulatory transformations performed by *E. lenta* (Alexander et al., 2021; Paik
657 et al., 2022), our results suggest that *E. lenta*'s effects on host immunity may be
658 multifaceted.

659 We elucidated the roles of three common gut metabolites in the metabolic
660 network of *E. lenta*: arginine, acetate, and agmatine. First, we confirmed that conversion
661 of arginine to ornithine is a core property of the *E. lenta* species. Production of ornithine
662 was the most consistent metabolic feature across strains and environments. Our stable
663 isotope analysis indicated that ornithine is primarily an end product of growth and is
664 relatively inaccessible as a carbon source for *E. lenta*. However, ornithine is a favorable

665 carbon and/or energy source for numerous other gut microbes (Noronha et al., 2018),
666 including as a substrate for Stickland metabolism by gut bacteria including
667 *Clostridioides difficile* (Girinathan et al., 2021; Liu et al., 2022; Pruss et al., 2022).
668 Therefore, production of ornithine by *E. lenta* may promote the growth of other
669 proteolytic bacteria in the surrounding gut ecosystem.

670 We also found that the presence of acetate has a dramatic effect on *E. lenta*
671 growth and metabolism *in vitro*. Acetate is a ubiquitous microbial metabolite in the
672 mammalian gut that varies in concentration (van der Hee and Wells, 2021). Previous
673 studies have speculated that *E. lenta* may produce acetate via autotrophic acetogenesis
674 (Harris et al., 2018; Hylemon et al., 2018). While our study does not resolve the
675 question of whether *E. lenta* has a functional acetogenic Wood-Ljungdahl pathway, we
676 found that environmental acetate is an important biosynthetic precursor for *E. lenta*,
677 incorporated partially via a distinctive bifurcated citric acid cycle (Amador-Noguez et al.,
678 2010; Huynen et al., 1999). If *E. lenta* is in fact an acetate consumer *in vivo*, as we have
679 observed *in vitro*, this role may have ecological consequences. For example, *E. lenta*
680 may compete for cross-fed acetate with other gut microbes, including the abundant,
681 health-linked members of the Firmicutes that metabolize acetate to butyrate at high
682 rates (Duncan et al., 2002; Muñoz-Tamayo et al., 2011). However, while we did not
683 identify any compound that can replace the role of acetate in *E. lenta*'s metabolic
684 network, the observation that *E. lenta* can grow to high carrying capacities in rich media
685 and in germ-free mice presumably lacking acetate indicates that other undetermined
686 compounds may be able to serve as equivalent carbon sources.

687 Finally, we identified agmatine as an alternate energy source for *E. lenta in vivo*.
688 Agmatine is a host metabolite with multiple roles as a neurotransmitter, regulator of
689 nitric oxide synthesis, and regulator and precursor of polyamine metabolism (Piletz et
690 al., 2013). Although agmatine can be synthesized at low levels by the host, particularly
691 in the brain, the gastrointestinal tract is thought to be a major source of systemic
692 agmatine (Haenisch et al., 2008)—sourced either directly from the diet and/or from
693 microbial metabolism. Dietary sources of agmatine include a variety of plant and animal
694 products, with the highest known levels in fermented foods and alcoholic beverages
695 (Galgano et al., 2012). Altered agmatine levels have been associated with a range of

696 diseases, including depression and diabetes (Piletz et al., 2013). Notably, reduced
697 agmatine levels in the gut have been linked to cell proliferation and cancer (Molderings
698 et al., 2004). Therefore, depletion of gastrointestinal agmatine by gut microbes including
699 *E. lenta* has the potential to impact host health and disease. Further work is needed to
700 clarify the roles of both production and degradation by gut microbes in regulation of host
701 agmatine metabolism.

702 Overall, our analysis of *E. lenta* nutrient dependencies revealed that this species
703 occupies a metabolic niche that is distinct from canonically described roles in the gut
704 ecosystem, such as primary and secondary carbohydrate degraders or conventional
705 methanogens and acetogens. *E. lenta* relies heavily on ATP generation from arginine
706 and/or agmatine catabolism, uses acetate as a key carbon source, and likely performs
707 anaerobic respiration with unknown and potentially diverse substrates. The carbon and
708 energy sources and auxotrophies that we identified were highly conserved across the *E.*
709 *lenta* species, with the exception of pantothenate. Knowledge of these conserved
710 metabolic dependencies may be an important tool in future therapeutic attempts to
711 engineer or modify *E. lenta* abundance, metabolic activity, and community interactions.
712 In addition, the resources described here, together with the development of tools for
713 genetic manipulation of *E. lenta*, may provide a basis for further investigation of the
714 biochemical and physiological mechanisms underlying its distinctive metabolic strategy.

715 Another resource generated by this study is a curated constraint-based genome
716 scale metabolic model of *E. lenta*. Constraint-based modeling is a promising approach
717 for predicting community interactions and ecosystem engineering (Heinken et al.,
718 2021a), but to date, community metabolic modeling tools have been difficult to validate
719 and have generated relatively limited insights beyond what could be obtained with
720 simpler annotation methods. Our analysis highlights the importance of phenotype-based
721 curation of individual reconstructions. Specifically, the initial semi-curated AGORA
722 model of *E. lenta* did not support any growth in EDM1 and lacked a complete version of
723 the agmatine deiminase pathway. Yet analysis of the more fully curated reconstruction
724 enabled us to confirm key reactions during growth with arginine and agmatine *in vitro*,
725 identify gaps representing potential novel enzymes, and uncover strain differences in
726 vitamin dependence. These results suggest that the quality and predictive power of

727 community metabolic models of the gut microbiota could be greatly improved by
728 systematic data generation and refinement of reconstructions for a metabolically diverse
729 sample of common taxa. Comparisons with growth in defined media conditions, -omics
730 data, and strain conservation can assist with model validation even when genetic tools
731 are not available.

732 Our approach combining untargeted metabolomics, genome-driven media
733 development, computational modeling, and gnotobiotic experiments may be a useful
734 strategy for accelerating scientific understanding of the biology of other understudied
735 microbes. Each of these model systems and data types produced a broadly useful
736 resource that partially supported findings from the others while also revealing novel
737 facets of *E. lenta* metabolism. Together, our study sheds light on the unusual metabolic
738 profile of an important member of the human gut microbiota, establishes a foundation
739 for future mechanistic studies of this organism, and demonstrates a generalizable
740 multidisciplinary approach to decipher the metabolic strategies of understudied
741 microbes.

742

743

744

745 **ACKNOWLEDGEMENTS**

746 We thank the UCSF Gnotobiotics Core staff (Jessie Turnbaugh, Kimberly Ly) for animal
747 care support and assistance. This work was supported by the National Institutes of
748 Health (2R01HL122593; 1R01AT011117; 1R01DK114034 to P.J.T., F32GM140808 to
749 C.N.). P.J.T. is a Chan Zuckerberg Biohub Investigator and held an Investigators in the
750 Pathogenesis of Infectious Disease Award from the Burroughs Wellcome Fund. We
751 acknowledge SeqCenter for assistance with RNA-Seq library preparation and
752 sequencing.

753

754 **AUTHOR CONTRIBUTIONS**

755 Conceptualization, C.N. and P.J.T.; Methodology, C.N., J.S., J.E.B., B.D., and P.J.T.;
756 Software, C.N., A.H., and I.T.; Formal Analysis, C.N., J.S., K.T., A.H., Y.L., and B.D.;
757 Investigation, C.N., J.S., J.E.B., V.E., M.A., Y.L., and B.D.; Data Curation, C.N., J.S.,
758 Y.L., D.D., and B.D.; Writing - Original Draft, C.N.; Writing - Review & Editing, C.N., J.S.,
759 J.E.B., V.E., M.A., K.T., A.H., Y.L., D.D., I.T., B.D., and P.J.T.; Visualization, C.N.;
760 Supervision, I.T., D.D., B.D., and P.J.T.

761

762 **DECLARATION OF INTERESTS**

763 P.J.T. is on the scientific advisory boards for Pendulum, Seed, and SNIPRbiome; there
764 is no direct overlap between the current study and these consulting duties. All other
765 authors have no relevant declarations.

766

767

768 **FIGURE TITLES AND LEGENDS**

769 **Figure 1. Production and depletion of diverse metabolites by *Eggerthella lenta*** 770 **DSM 2243 in chemically defined media. A)** Number of metabolite features detected

771 by tandem LC-MS in culture samples at each time point. Features are considered
772 present if their average peak height in supernatant is greater than 3x the average peak
773 height in blank samples. Using both positive and negative ionization modes, an
774 increasing number of features not found in controls appear in culture supernatants over
775 time. **B)** Number of differentially abundant metabolite features compared with sterile
776 control media at each time point, based on FDR-adjusted t-tests of log-transformed
777 peak heights. **C)** Volcano plot of differentially abundant metabolite features at the final
778 time point (50 hours) compared with sterile controls. p -values shown on the y -axis are
779 based on Welch's t-tests comparing values at the final time point vs. sterile controls
780 (Benjamini-Hochberg adjusted). **D)** Heatmap of individual metabolite trajectories in
781 cultures of *E. lenta* DSM 2243 grown in EDM1 batch culture. Features shown are those
782 whose abundance was significantly different from controls (FDR-adjusted $p < 0.1$ and
783 absolute \log_2 fold change > 0.75) at the final time point. Identified metabolites are
784 labeled; the number in parentheses indicates the Metabolomics Standards Initiative
785 confidence level for that identification (with 1 as highest confidence, see Methods).
786 Values shown are average log-transformed peak heights, scaled for each feature. The
787 gray heatmap at the top indicates the average batch culture density at each time point
788 of *Eggerthella lenta* DSM 2243 in EDM1 (normalized OD600). See also [Figure S1-2](#),
789 [Table S1-2](#).

790 791 **Figure 2. *E. lenta* uses acetate for nucleotide and peptidoglycan biosynthesis. A)**

792 Growth of *E. lenta* DSM 2243 in EDM1 media with varying concentrations of sodium
793 acetate. **B)** Growth of *E. lenta* DSM 2243 in EDM1 media in which 1 mM sodium
794 acetate is replaced with other small carbon compounds. **C)** Trajectories of identified
795 metabolite features responsive to acetate concentration in *E. lenta* EDM1 batch
796 cultures. Values are scaled average log-transformed peak heights from untargeted
797 metabolomics profiling of supernatants. Labels show metabolite identity and MSI
798 confidence level in parentheses. Metabolites shown are those that were assigned an

799 identity and that had significantly different trajectories in the 0 mM vs. 1 mM acetate
800 group based on spline regression comparison with the R package *santaR* (FDR-
801 adjusted $p < 0.25$). **D)** Stable isotope-resolved metabolomics profiling of *E. lenta* DSM
802 2243 in EDM1 media with $^{13}\text{C}_2$ labeled acetate. The number of compounds with labeled
803 isotopologues detected at a peak area $> 10^5$ is shown for each sample group and time
804 point, indicating incorporation of acetate into varied metabolites by *E. lenta*. **E)** Mass
805 isotopologue distributions (MIDs) of intracellular metabolites. Each barplot shows the
806 average isotopologue distribution in 1 mM and 10 mM acetate cultures. Compounds
807 shown are those with an average labeled MID > 0.15 and a total peak area from labeled
808 isotopologues of at least 10^4 in at least one *E. lenta* DSM 2243 labeled acetate
809 condition. **F)** Hypothesized pathways for incorporation of acetate into *E. lenta* central
810 carbon metabolism and into biosynthetic pathways to produce labeled metabolites.
811 Circles indicate the number of carbon atoms in selected compounds and are colored
812 green to indicate incorporation of ^{13}C isotopes from external acetate. Compound names
813 in bold were detected with the observed labeling patterns in either intracellular
814 metabolite extracts or culture supernatants. Corresponding enzymes are annotated in
815 the *E. lenta* DSM 2243 genome for all reactions shown, and labeled in gray with the
816 NCBI locus tag number. For pathways shown at a summary level (gluconeogenesis,
817 pentose phosphate pathway, purine and pyrimidine biosynthesis, peptidoglycan
818 biosynthesis), only the first enzyme in the pathway is labeled on the plot. See also
819 [Figure S3-5, Data S1](#).

820
821 **Figure 3. A curated genome-scale metabolic model of *E. lenta* DSM 2243 partly**
822 **explains growth phenotypes across conditions.** **A)** Summary of the curated
823 reconstruction of *E. lenta* DSM 2243 indicating the number of genes, reactions, and
824 metabolites in the original and curated models, and the share of those required to be
825 active for growth in EDM1 based on parsimonious flux balance analysis (pFBA). **B)**
826 Summary of the total number of reactions by subsystem, and the share of each
827 subsystem predicted to be active in EDM1 (only the top 20 subsystems are shown). **C)**
828 Acetate and L-arginine uptake dependencies inferred by the model. In the final curated
829 model (red lines), the maximum growth rate decreases with decreasing availability of

830 both L-arginine and acetate, qualitatively consistent with experimental data. A previous
831 model incorporating a carbon monoxide dehydrogenase reaction based on (Harris et al,
832 2018) (blue lines) failed to recapitulate the expected dependencies. **D)** Confusion matrix
833 summarizing a comparison of growth/no growth between the iEL2243_2 model vs.
834 experimental observations for leave-one-out media conditions. **E)** Full set of quantitative
835 comparisons underlying panel D. Each column shows the FBA-inferred maximum
836 growth rate in the EDM1 condition with a media component removed, paired with the
837 experimentally observed area under the empirical growth curve for that condition. A
838 gray tile indicates zero growth. **F)** Comparison of shifts in metabolomics data with
839 uptake and secretion rate ranges inferred for the same compounds by flux variability
840 analysis (FVA). Metabolites that can only be imported according to FVA were
841 decreased in metabolomics data, while those with potential for being produced were
842 indeed produced. **G)** Comparison of absolute fluxes inferred by pFBA with gene
843 expression of linked enzymes of *E. lenta* DSM 2243 during exponential growth in
844 EDM1. Within flux quantiles (on the x-axis), genes are expressed at a wide range of
845 levels, but genes linked to reactions with the highest fluxes are generally highly
846 expressed. See also [Figure S6](#), [Table S3-4](#).

847
848 **Figure 4. Extensive within-species variation in *E. lenta* metabolites can be linked**
849 **to variable gene families. A)** Volcano plot of metabolite features detected in stationary
850 phase supernatants of *E. lenta* DSM 2243 (UCSF lab strain) vs. sterile controls. *P*-
851 values are based on Benjamini-Hochberg corrected Welch's t-tests. Features are
852 colored based on whether their classification as significantly produced or depleted
853 (increased or decreased with FDR-adjusted p -value <0.1 and $\log_2\text{FC}>0.5$) is consistent
854 across 28 other *E. lenta* isolates and one isolate of *Eggerthella sinensis* profiled in the
855 same experiment. **B)** Procrustes analysis of overall metabolite profiles compared with
856 genome features. The upper plot shows a rotated Procrustes superimposition of
857 average metabolite profiles for each isolate (red points) and the phylogenetic distance
858 between them based on an alignment of core genes (blue points). The lower plot shows
859 a superimposition of metabolite profiles and profiles based on the presence/absence of
860 variable gene clusters (purple points). **C)** The left-hand panel shows the distribution of

861 strain-variable features in various ClassyFire chemical superclasses, based on Feature-
862 based Molecular Networking with GNPS. The number in parentheses for each class
863 indicates the total number of features with that assignment. The right-hand panel shows
864 the number of strains producing a given feature, among features produced by any
865 *Eggerthella* isolate. Each point represents a single feature, and its position on the x-axis
866 indicates the number of strains for which that feature was significantly increased (FDR-
867 adjusted p -value < 0.1 and \log_2 fold change > 0.5) in supernatants compared with
868 controls. Superclasses (y-axis labels) are the same as in panel C. **E)** Feature
869 abundances of example metabolites across strains. The first two panels show two
870 strain-variable unidentified features associated with the presence of specific strain-
871 variable gene families - putatively identified as the two dominant naturally occurring
872 isotopes of an [M+Cl-] adduct of the teichoic acid component ribitol. The points indicate
873 the log-transformed abundances of these features for each strain. The dotted line in
874 each panel indicates the average level of that feature in sterile controls. Points in dark
875 blue represent strains whose genomes contain genes for a ribitol-5-phosphate
876 cytidyltransferase (*tarJ*) and ribulose-5-phosphate reductase (*tarI*) not found in other
877 genomes. The third and fourth panels show a highly conserved identified metabolite
878 (ornithine) compared with a strain-variable identified metabolite (pantothenic acid).
879 Points in white in the pantothenic acid panel indicate strains whose genome lacks the
880 final step in the biosynthetic pathway for this metabolite. Points are shown as mean and
881 standard error across three replicates. The order of strains on the y-axis matches their
882 phylogeny, shown in [Figure S7A](#). **F)** Strains lacking a gene annotated as pantothenate
883 synthetase deplete pantothenic acid completely from media (previous panel) and have a
884 substantial growth defect when grown in the absence of pantothenic acid (left panel).
885 Closely related strains that do possess this gene are unaffected by removal of
886 pantothenic acid (right panel). Carrying capacity is estimated based on a logistic growth
887 model fit by the R package *growthcurver*. See also [Figure S7](#), [Table S5-6](#).

888

889 **Figure 5. Comparison between *E. lenta*'s metabolic footprint *in vivo* and *in vitro***
890 **reveals shared metabolite signatures. A)** Principal component analysis of untargeted
891 metabolomics profiles of intestinal contents and of serum. **B)** Comparison of the effect

892 of *E. lenta* on metabolite features detected in both EDM1 cultures and monoclonized
893 mice. Each point represents a metabolite feature detected in both datasets. The *x*-axis
894 indicates the \log_2 fold change of each feature in supernatants compared with sterile
895 controls, compared with the estimated \log_2 fold change of that feature in monoclonized
896 mice compared with germ-free mice. Points are colored green if the feature is
897 significantly differentially abundant in gnotobiotic mice and is shifted in the same
898 direction by the corresponding strain in the stationary phase *in vitro* experiment. See
899 also [Figure S8](#), [Data S2](#).

900

901 **Figure 6. Agmatine can replace arginine as an energy source for *E. lenta*. A)**
902 Identified metabolite features with the highest estimated effects in *E. lenta* DSM 2243-
903 colonized mice compared with germ-free. Each point indicates the effect size of that
904 feature in a particular sample site (denoted by shape). **B)** Model of the agmatine
905 deiminase ATP-generating pathway (Llácer et al., 2007). Three copies of an operon
906 containing genes for all three of the labeled proteins are annotated in the *E. lenta* DSM
907 2243 genome. **C)** Growth of *E. lenta* DSM 2243 in EDM1 where arginine has been fully
908 or partially replaced with agmatine sulfate. Curves show mean \pm standard error for four
909 replicates. **D)** Induction of the agmatine deiminase pathway in *E. lenta* DSM 2243
910 cultures in response to the addition of agmatine. The volcano plot shows the \log_2 fold
911 change and FDR-adjusted *p*-values of agmatine-treated cultures compared to vehicle
912 (as estimated by negative binomial differential abundance models with DESeq2). See
913 also [Figure S9](#), [Table S7](#).

914

915

916 **STAR METHODS**

917 **RESOURCE AVAILABILITY**

918 **Lead contact**

919 Further information and requests for resources and reagents should be directed to the
920 Lead Contact Peter Turnbaugh (Peter.Turnbaugh@ucsf.edu).

921

922 **Materials availability**

923 This study does not contain newly generated materials.

924

925 **Data and code availability**

926 RNA sequencing data has been deposited in NCBI GEO and are publicly
927 available as of the date of publication. Metabolomics datasets have been deposited in
928 Metabolomics Workbench and are publicly available as of the date of publication.
929 Processed metabolomics datasets, growth data, and metabolic reconstructions are
930 available from Zenodo and are publicly available as of the date of publication.
931 Accession numbers and DOIs are listed in the key resources table.

932 All original code has been deposited at Zenodo and GitHub
933 (https://github.com/turnbaughlab/2022_Noecker_ElentaMetabolism) and is publicly
934 available as of the date of publication. DOIs are listed in the key resources table.

935 Any additional information required to reanalyze the data reported in this paper is
936 available from the lead contact upon request.

937

938 **EXPERIMENTAL MODEL AND SUBJECT DETAILS**

939 **Mouse husbandry and experiments**

940 Mouse samples analyzed in this study were collected and described previously in
941 (Alexander et al., 2021). The mouse experiment was approved by the University of
942 California San Francisco Institutional Animal Care and Use Committee. The mice were
943 housed at temperatures ranging from 67-74°F and humidity ranging from 30-70%
944 light/dark cycle 12hr/12hr. LabDiet 5021 chow was used. No mice were involved in
945 previous procedures before experiments were performed. Mice were assigned to
946 groups to achieve similar age distribution between groups.

947 C57BL/6J mice (males, ages 4-8 weeks) were obtained from the University of
948 California, San Francisco Gnotobiotics core facility (gnotobiotics.ucsf.edu) and housed
949 in Iso positive cages (Tecniplast). Mice were colonized via oral gavage with *E. lenta*
950 monocultures (10^9 CFU/mL, 200 μ l gavage) and colonization was confirmed via
951 anaerobic culturing and/or qPCR for an *E. lenta* specific marker (*elnmrk1*) (Bisanz et al.,
952 2020; Koppel et al., 2018). Mice were colonized for 2 weeks prior to sacrifice and
953 sample collection.

954

955 **Bacterial strains**

956 Strain isolates analyzed in this work are described in (Bisanz et al., 2020). All
957 experiments were performed in an anaerobic chamber with 2-5% hydrogen gas, 20%
958 carbon dioxide, and the balance nitrogen, with growth in a 37°C incubator. Standard
959 BHI media (VWR 90003-040) supplemented with 1% L-arginine (referred to below as
960 BHI+) was used for culturing outside of defined media experiments.

961

962 **METHOD DETAILS**

963 **Defined media formulations and preparation**

964 Standard composition of the EDM1 media and related formulations are provided
965 in [Table S1](#). As specified in [Table S1](#), some experiments were performed using the
966 initial formulation of the media, and others using a simplified form based on the results
967 of leave-one-out growth experiments. For most components, 30-1000x stock solutions
968 were prepared following (Zhang et al., 2009). Stock solutions were sterilized with a 0.22
969 μ m syringe filter and stored at -20°C. Amino acids were typically added together directly
970 from powder into a combined 2x stock solution which was then filter sterilized with a
971 0.22 μ m vacuum filter, except when preparing individual leave-one-out amino acid
972 growth experiments. Most versions used ATCC Trace Mineral and Vitamin Mix
973 Supplements (MD-TMS and MD-VS), except for experiments to test leaving out
974 individual components of these mixes. Individual replacement components are specified
975 in [Table S1](#). Media formulations were allowed to equilibrate in an anaerobic chamber
976 (Coy) for at least 24 hours prior to use.

977

978 **Bacterial culture and growth assays**

979 For growth and metabolomics experiments, glycerol stocks were first streaked on
980 BHI+ agar plates and incubated at 37°C for 2-3 days. Individual colonies were
981 inoculated into 3-4 mL liquid BHI+ and incubated at 37°C for 40-48 hours, or until
982 approximately early stationary phase. Culture optical density (600 nm wavelength
983 absorbance, OD₆₀₀) was measured using a Hach DR1900 spectrophotometer. 1 mL
984 samples of BHI starter cultures were then centrifuged at 1,568 rcf for 4 minutes in a
985 microcentrifuge (ThermoScientific mySpin 12) in the anaerobic chamber and
986 resuspended in 1 mL sterile phosphate-buffered saline (PBS). For leave-one-out
987 experiments, the resuspended cells were washed by centrifuging and resuspending in
988 PBS again. The resulting suspension was vortexed and diluted to an approximate
989 OD₆₀₀ of 0.1, and used as inoculum into defined experimental conditions.

990 Growth assays were performed in standard 96-well microplates (Corning) at
991 37°C with a microplate reader (Biotek Eon or PowerWave). 180 µL of defined media
992 were pipetted into each well, followed by 20 µL of inoculum. All experiments included at
993 least three sterile control wells for each condition, into which 20 µL of sterile PBS was
994 pipetted to establish consistent background OD₆₀₀ measurements. Replicate wells
995 were distributed pseudorandomly across the plate to control for plate layout effects, and
996 inoculated wells were always paired with an adjacent control well of the same condition.
997 3-6 replicates were included for each condition. Plates were sealed with a transparent
998 Breathe-Easy sealing gas exchange membrane (RPI). Every 30 minutes, plates were
999 shaken at medium speed for 40 seconds, after which OD₆₀₀ readings were performed.

1000 After large metabolomics and RNA-Seq experiments (see below), culture purity
1001 was checked by plating and 16S rRNA gene Sanger sequencing, using standard
1002 primers (8F AGAGTTTGATCCTGGCTCAG and 1542R
1003 AAGGAGGTGATCCAGCCGCA).

1004

1005 **Sample collection for metabolomics**

1006 Time course experiments were conducted in tubes in the anaerobic chamber in a
1007 37°C incubator. For all metabolomics experiments, three independent culture replicates
1008 were included for each condition, with an equal number of uninoculated control tubes.

1009 Starter cultures and inocula were prepared as described above for growth assays. 5mLs
1010 of defined media was added to VWR glass culture tubes (53283-800) with screw caps.
1011 The PBS-washed inoculum was added to culture tubes to obtain an approximate
1012 starting OD600 of 0.001. A preliminary growth assay was conducted to define time
1013 points spanning the exponential growth phase in the tested conditions. At each time
1014 point, OD600 measurements of all inoculated tubes were first measured using a Hach
1015 DR1900 spectrophotometer, with a paired control tube to normalize for the background.
1016 100 μ L from each tube were then transferred into a 96-well microplate, which was
1017 sealed and removed from the anaerobic chamber. Plates were centrifuged at 1,928 rcf
1018 at 4°C for 8 minutes, after which supernatants were collected into fresh polypropylene
1019 tubes or plates, sealed, and flash-frozen in liquid nitrogen.

1020 Two time course experiments were carried out with stable isotope-labeled
1021 substrates. Experimental groups included conditions in which sodium acetate in the
1022 defined media was replaced with $^{13}\text{C}_2$ labeled sodium acetate (Sigma-Aldrich 282014),
1023 along with a matched experimental group with the same concentration of unlabeled
1024 substrate. The same procedure was followed for the arginine labeling experiment, using
1025 $^{13}\text{C}_6$ labeled L-arginine HCl (Sigma-Aldrich 643440).

1026 For the comparative strain metabolomics experiment, 96-well polypropylene
1027 deep well plates were prepared with 800 μ L of fresh media in each well. Starter cultures
1028 and inocula for 29 isolates of *Eggerthella lenta* and 1 isolate of *Eggerthella sinensis*
1029 (Bisanz et al., 2020) were prepared as described above for growth assays, except
1030 without final dilution, and 80 μ L was used to inoculate wells, leaving a blank well in
1031 between every culture well to prevent cross-contamination. After 72 hours, OD600
1032 measurements were taken, plates were centrifuged, and supernatants were collected as
1033 described above.

1034

1035 **Targeted quantification of acetate**

1036 A subset of unlabeled supernatant samples from the acetate labeling time course
1037 were shipped to Stanford University on dry ice for targeted quantification of acetate.

1038 Samples (20 μ L) were first mixed with an internal standard solution (30 μ L; 1 mM
1039 phenylpropionate-d9) in a V-bottomed, poly(propylene), 96-well plate, and extracted by

1040 mixing with 3 sample volumes of extraction solution (75% acetonitrile:25% methanol).
1041 The plate was covered with a lid and centrifuged at 5,000 rcf for 15 min at 4°C.
1042 Supernatant was collected for derivatization before subjecting to LC–MS analysis.

1043 Samples were processed using a derivatization method targeting compounds
1044 containing a free carboxylic acid. Extracted samples were mixed with 3-
1045 nitrophenylhydrazine (NPH; 200 mM in 50% acetonitrile) and N-(3-
1046 dimethylaminopropyl)-N'-ethylcarbodiimide (120 mM in 6% pyridine) at a 2:1:1 ratio.
1047 The plate was sealed with a plastic sealing mat (Thermo Fisher Scientific, #AB-0566)
1048 and incubated at 40°C, 600 rpm in a thermomixer for 60 min to derivatize the
1049 carboxylate-containing compounds. The reaction mixture was quenched with 0.02%
1050 formic acid in 10% acetonitrile:water before LC–MS.

1051 Samples were injected via refrigerated autosampler into mobile phase and
1052 chromatographically separated by an Agilent 1290 Infinity II UPLC and detected using
1053 an Agilent 6545XT Q-TOF (quadrupole time of flight) mass spectrometer equipped with
1054 a dual jet stream electrospray ionization source, operating under extended dynamic
1055 range (1,700 m/z). Chromatographic separation was performed using an ACQUITY
1056 Bridged Ethylene Hybrid (BEH) C18 column 2.1 x 100 mm, 1.7-micron particle size,
1057 (Waters Corp. Milford, MA), using chromatographic conditions published elsewhere (Liu
1058 et al., 2022). MS1 spectra were collected in centroid mode, and peak assignments in
1059 samples were made based on comparisons of retention times and accurate masses
1060 from authentic standards using MassHunter Quantitative Analysis v.10.0 software from
1061 Agilent Technologies. Acetate was quantified from calibration curves constructed with
1062 acetate-d4 as a standard using isotope-dilution MS with phenylpropionate-d9 as the
1063 internal standard. Calibration curves were performed in a modified base form of EDM1
1064 lacking amino acids and other carboxylic acids. A background level of 1.05 mM of
1065 acetate was subtracted to obtain the final quantities.

1066 A plate layout error for supernatant samples from time points 4-7 in this
1067 experiment was noted based on the resulting acetate concentrations and corrected
1068 across datasets.

1069

1070 **Untargeted metabolomics**

1071 Bacterial culture supernatant and sterile media, used in culture, were thawed on
1072 wet ice. Once thawed, samples were homogenized by inversion five times. Extracellular
1073 culture supernatant samples were prepared as follows: 20 μ L of culture supernatant
1074 were extracted using 80 μ L of a chilled extraction solvent at -20°C (1:1
1075 acetonitrile:methanol, 5% water containing stable isotope-labeled internal standards).
1076 Samples were homogenized via pipette action, incubated for 1 hour at -20°C ,
1077 centrifuged at 4°C at 6000 rcf for 5 min. The supernatant was transferred to a new plate
1078 and immediately sealed and kept at 4°C prior to prompt analysis via LC-MS/MS.

1079 Intestinal samples (colon, cecum, ileum) were prepared individually using a
1080 single protocol as follows. Samples were kept frozen on dry ice and massed to at least
1081 10 mg. Four microliters of -20°C extraction solvent (2:2:1 methanol:acetonitrile:water +
1082 stable isotope labeled internal standards) were added per milligram of intestinal sample.
1083 Six to eight 1mm zirconia silica beads were added to each sample followed by prompt
1084 bead beating (15 Hz, for 10 minutes). Following a 1 hour incubation in the -20°C
1085 freezer, samples were centrifuged at 4°C at 18,407 rcf for 5 minutes. Supernatant was
1086 collected and stored at -20°C prior to centrifugal plate filtration (0.2 micron
1087 polyvinylidene difluoride (PVDF) Agilent Technologies, Santa Clara CA) at 4°C at 4,122
1088 rcf for 3 min. Collection plate was sealed and maintained at 4°C prior to prompt
1089 analysis.

1090 Serum samples were first thawed on wet ice. 20 μ L of serum was extracted with
1091 4 volumes of methanol, containing stable isotope labeled internal standards. Samples
1092 were homogenized by vortexing for 20 seconds and placed in a -20°C for 1 hour to
1093 maximize protein precipitation. After freezer incubation, samples were centrifuged at
1094 4°C at 18,407 rcf for 5 minutes. Supernatant was removed and dried under vacuum via
1095 centrivap (Labconco Corp.). Dried samples were then resuspended in 30 μ L of 80%
1096 acetonitrile in water containing exogenous standard CUDA at 60 ng/mL. Samples were
1097 maintained at 4°C prior to prompt analysis.

1098 Within each analysis batch, a small amount of each sample was removed and
1099 combined to create multiple technical replicate 'pools' which were analyzed
1100 intermittently throughout the analysis. These pools were used as external standards to

1101 ensure instrument stability across the batch. Additionally, method blanks were created
1102 using LC-MS grade water in place of supernatant, sterile media, serum, or intestinal
1103 contents. These blanks were used to ensure that reported metabolites were not
1104 inadvertently added during sample preparation.

1105 Samples, sterile media, pools, and blanks were promptly added to a Thermo
1106 Vanquish Autosampler at 4°C in a Vanquish UHPLC (Thermo Fisher Scientific,
1107 Waltham, MA). Chromatographic separation was performed using an ACQUITY Bridged
1108 Ethylene Hybrid (BEH) Amide column 2.1 x 150 mm, 1.7-micron particle size, (Waters
1109 Corp. Milford, MA), using chromatographic conditions published elsewhere (Lai et al.,
1110 2018). Samples were analyzed on a Thermo Q-Exactive HF orbitrap mass spectrometer
1111 operated utilizing data dependent acquisition of MS2. Data was acquired independently
1112 in positive and negative modes via subsequent injections.

1113

1114 **SIRM metabolomics**

1115 Intracellular extract samples were prepared with the following procedure, which
1116 was optimized for lysis of thick gram-positive cell walls: 600 µL of culture was
1117 transferred to an Eppendorf tube in anaerobic conditions and subsequently centrifuged
1118 at 10,000rcf for three minutes at 4°C, after which the supernatant was removed and the
1119 samples were immediately flash frozen to quench metabolites. 300 µL of cold methanol
1120 was then added to each pellet, followed by sonication on ice for 5 minutes and then
1121 shaking at 4°C for 4-12 hours. Samples were then centrifuged at 4°C at 15,000 rcf for 8
1122 minutes, after which 120 µL of supernatant was transferred to fresh tubes and stored at
1123 -80°C until analysis. Prior to analysis, intracellular samples were dried at room
1124 temperature via Centrivap Benchtop Concentrator (Labconco Corp.). Samples were re-
1125 suspended in 60 µL of a chilled solution of 1:1 methanol and acetonitrile, with 24%
1126 water at -20°C containing the internal standards CUDA and VAL-TYR-VAL each at 60
1127 ng/mL. Samples were centrifuged at 4°C, 4,122 rcf for 5 minutes and the supernatant
1128 transferred to a vial and immediately capped for LC-MS analysis.

1129 Extracellular supernatant extraction for SIRM metabolomics was performed as
1130 described above (Untargeted metabolomics section) with one modification. In SIRM
1131 samples, deuterated internal standards were replaced with CUDA and Val-Tyr-Val to

1132 enable untargeted enrichment analysis. LC-MS/MS analysis conditions for SIRM
1133 metabolomics were identical to those used for standard untargeted metabolomics.

1134

1135 **Untargeted metabolomics data processing**

1136 Untargeted metabolomics datasets were processed using MS-DIAL version 4.60
1137 (Tsugawa et al., 2015). Metabolite features with intensity not greater than 3-fold
1138 elevated in samples compared to mean blank intensity were removed. Annotations were
1139 assigned using both local (Han et al., 2021) and global (Mass Bank of North America)
1140 tandem mass spectral libraries. Annotation confidence scores were assigned based on
1141 Metabolomics Standards Initiative (MSI) best practices (Fiehn et al., 2007; Schymanski
1142 et al., 2014). Briefly; MSI level 1 denotes library matches of accurate mass (m/z),
1143 retention time (RT) and tandem mass spectra (MS2). MSI level 2 follows the same rules
1144 as MSI 1, but allows for partial matching of MS2 spectra - as is prone to occur when
1145 experimental spectra are convoluted. MSI level 3 denotes a high scoring and visually
1146 confirmed match of MS2 spectra. MSI level 4 is assigned when exact stereospecificity
1147 cannot be determined by MS2 and chromatographic separation. MSI level 4 is often
1148 assigned to sugars, lipids, and polyphenols. MSI levels 1 and 2 could only be assigned
1149 to metabolites in our local library, for which authentic standards have been analyzed in
1150 the same chromatographic conditions as the samples being annotated. Post processing
1151 was performed using MS-FLO (DeFelice et al., 2017) for removal of erroneous features.

1152 Processed datasets were further analyzed using Feature-based Molecular
1153 Networking and MolNetEnhancer in the GNPS web platform (Djombou Feunang et al.,
1154 2016; Ernst et al., 2019; Nothias et al., 2020; Wang et al., 2016), which assigned
1155 ClassyFire chemical classes to features based on molecular networking, independently
1156 of whether they were assigned a library identity.

1157 To merge positive and negative ionization mode datasets from the same
1158 samples, duplicate features across datasets were identified as those with an expected
1159 mass difference of less than 0.02, a retention time difference of less than 0.1, and a
1160 Pearson correlation across samples of at least 0.7. If one or both members of a pair of
1161 duplicate features were assigned an identification, the feature with lower (more

1162 confident) MSI score was retained in the merged dataset. Otherwise, the positive mode
1163 feature was retained. The other feature was removed for downstream analysis.

1164 Prior to statistical analysis, initial untargeted metabolomics feature tables were
1165 filtered to remove features with a high coefficient of variation across replicate samples
1166 (> 50%) and to remove potential technical outlier samples where the total signal from all
1167 features differed from the assay median by > 50%. Log₁₀-transformed intensities were
1168 used for most statistical analysis, with the exceptions of SIRM datasets and the
1169 comparative strains dataset (for which values were approximately normally distributed
1170 without transformation). A pseudocount equal to 0.25 times the minimum non-zero
1171 value was added to the peak intensities for each feature before log transformation.
1172 Heatmaps of metabolite abundances were generated using the *ComplexHeatmap*
1173 package (Gu et al., 2016).

1174

1175 **SIRM data processing**

1176 Intra- and extracellular untargeted data generated from SIRM experiments was
1177 analyzed separately using *Compound Discoverer* version 3.3 (Thermo Scientific,
1178 Bremen, Germany). Samples treated with labeled compounds were always paired with
1179 matched samples treated with unlabeled compounds in order to correct for naturally
1180 occurring isotope abundances. Unlabeled samples were used for compound detection
1181 and formula assignment via isotope pattern-based prediction, spectral library matches,
1182 or mass lists matches. The isotope patterns and formulas from the sample files then
1183 served as a reference for the detection of potential isotopologues per compound in the
1184 labeled sample type.

1185 Specifically, the workflow consisted of the following nodes in Compound
1186 Discoverer: *Input Files*→ *Select Spectra*→ *Align Retention Times (ChromAlign)*→
1187 *Detect Compounds (Legacy)* → *Group Compounds*→ *Predict Compositions*→ *Search*
1188 *Mass Lists*→ *Search mzCloud*→ *Mark Background Compounds*→ *Assign Compound*
1189 *Annotations*→ *Analyze Labeled Compounds*→ *Descriptive Statistics*→ *Differential*
1190 *analysis*.

1191 The default settings from the “Stable Isotope Labeling w Metabolika Pathways
1192 and ID using Online Databases” workflow were used, with the following modifications:

- 1193 (1) Detect Compounds (Legacy): General– Min.Peak Intensity: 10000; Ions:
1194 [M+H]⁺+1 or [M-H]⁻-1 for positive and negative mode experiments respectively.
- 1195 (2) Group Compounds: Peak Rating Filter– Peak Rating Threshold: 4; Number of
1196 Files: 3.
- 1197 (3) Search Mass Lists: Search Settings– Mass Lists: Combined Hilic Mass mzRT
1198 library; Use Retention Time: True; RT Tolerance: 0.3 min; Mass Tolerance: 5
1199 ppm.
- 1200 (4) Search mzCloud: DDA Search– Match Factor Threshold: 85
- 1201 (5) Mark Background Compounds: General– Max. Sample/Blank: 3
- 1202 (6) Assign Compound Annotations: Data Sources– Data Source #1: mzCloud
1203 Search; Data Source #2: MassList Search; Data Source #3: Predicted
1204 Compositions.
- 1205 (7) Analyze Labeled Compounds: Pattern Analysis– Intensity Threshold [%]: 2

1206

1207 Positive and negative polarity files were analyzed initially as separate studies
1208 with the following study definitions: Study factors including strain, replicate, substrate
1209 concentration, sample type, and time point were assigned. Sample types were assigned
1210 as either sample (unlabeled), labeled, or blank. These study factors interfaced with
1211 several nodes to reduce undesirable features and maximize reporting of quality high
1212 intensity peaks with potential for accurate measurement of ¹³C incorporation.

1213 Results were filtered for non-blank formula assignment and absence in
1214 background samples. The MSI levels and labeling status for persisting entries were
1215 manually inspected for each compound and annotated onboard via custom tags. MSI
1216 levels were assigned based on the criteria previously described to match MS-Dial
1217 output. The mass isotopologue distributions were plotted to ensure reproducibility
1218 between replicates of various time points and detect anomalous labeling trends. The
1219 absence of reported enrichment in control samples processed as labeled samples was
1220 verified. A minimum threshold of 3% combined enrichment across all isotopologues
1221 other than M+0 was applied. This threshold was necessary for less abundant peaks
1222 where the ¹³C natural isotopic abundance correction introduces uncertainty in the M+1
1223 and M+2 isotopologues.

1224 A specification of the full Compound Discoverer workflow is available at
1225 https://github.com/turnbaughlab/2022_Noecker_ElentaMetabolism.

1226

1227 **RNA-Seq**

1228 *E. lenta* DSM 2243 glycerol stocks were plated on BHI+ and incubated
1229 anaerobically at 37°C for three days. A single colony was then inoculated into 5mLs of
1230 BHI+ liquid culture and incubated at 37°C for 48 hours. 1 mL of the resulting culture was
1231 then centrifuged, washed once, and resuspended in equal volume PBS; all in anaerobic
1232 conditions. 220 µL of this inoculum were transferred into culture flasks containing 20 mL
1233 of EDM1 (70% carbon source reduced version, see **Table S1**) to obtain a starting
1234 OD600 of 0.01. After 20 hours of growth (early or mid-exponential phase), these
1235 cultures were treated with an additional 1.9 mL of sterile water or filter-sterilized solution
1236 containing either L-arginine (to reach a final concentration of 86 mM), sodium acetate
1237 (final concentration of 14.5 mM), or agmatine sulfate (final concentration of 30 mM).
1238 After 18 more hours (late exponential phase), 7.5 mL of each culture was collected into
1239 15 mL conical tubes containing 5 mL of Qiagen Bacterial RNA-Protect (#76506).
1240 Cultures were centrifuged at 2,800 rcf at 4°C for 10 minutes, after which the supernatant
1241 was carefully removed. Pellets were extracted directly using the Qiagen RNeasy Mini kit
1242 (#74104) with modifications for difficult-to-lyse Gram positive bacteria. Samples were
1243 maintained on ice throughout the protocol. Briefly, 200 µL of TE buffer containing
1244 lysozyme (15mg/mL, #L4919) and 20 µL of Qiagen Proteinase K (#19131) were added
1245 to each pellet, vortexed gently, and incubated at room temperature for 10 minutes with
1246 shaking on an Eppendorf ThermoMixer at 900 rpm. 700 µL of Buffer RLT was then added
1247 to each tube and vortexed, after which the full contents were transferred to MP
1248 Biomedical Lysing Matrix E tubes (#116914500) and disrupted mechanically in a
1249 BioSpec Mini-Beadbeater-96 for 50 seconds. After disruption, tubes were centrifuged
1250 for three minutes at 15,000rcf and 850 µL of supernatant was transferred to fresh tubes.
1251 590 µL of 80% ethanol was added to each sample and mixed by pipetting, after which
1252 lysates were transferred to Qiagen RNeasy spin columns and washed, following the
1253 RNeasy Mini kit QuickStart protocol including a single on-column DNase digestion
1254 (DNase #79254). After purification, RNA was eluted twice into 30 µL of nuclease-free

1255 water. RNA integrity was checked using an Agilent TapeStation 4150 and stored at -
1256 80°C.

1257 RNA library preparation and sequencing was performed by the Microbial
1258 Genome Sequencing Center/SeqCenter. Samples were DNase treated with Invitrogen
1259 DNase (RNase free, #AM2222). Library preparation was performed using Illumina's
1260 Stranded Total RNA Prep Ligation with Ribo-Zero Plus kit (#20040529) and 10bp IDT
1261 for Illumina indices. Supplementary oligonucleotide probes specific to *E. lenta* rRNA and
1262 other highly expressed noncoding RNAs were incorporated during Ribo-Zero depletion
1263 (**Table S10**). Sequencing was done on a NextSeq 2000 with 2x50bp reads.
1264 Demultiplexing, quality control, and adapter trimming was performed with bcl-convert
1265 v3.9.3.

1266 Reads were trimmed and quality filtered using *fastp* v0.20.0 (Chen et al., 2018)
1267 with the following parameters: `--trim_poly_g --cut_front --cut_tail --cut_window_size 4 --`
1268 `cut_mean_quality 20 --length_required 15`. The Hisat2 aligner v2.2.1 (Kim et al., 2019)
1269 was used to map reads to the *E. lenta* DSM 2243 reference genome, downloaded from
1270 NCBI RefSeq (GCF_000024265.1). Gene-level read counts were obtained using the
1271 corresponding NCBI annotations and the *featureCounts* function in the R package
1272 *Rsubread* v2.6.4 (Liao et al., 2019), with the minimum quality score set to 1.

1273

1274 **Construction, curation, and analysis of metabolic reconstructions**

1275 Genome-scale metabolic reconstructions were created from genome sequences
1276 of 25 *E. lenta* strains (Bisanz et al., 2020) using the DEMETER pipeline (Heinken et al.,
1277 2020, 2021b). Briefly, DEMETER performs systematic refinement of a draft genome-
1278 scale reconstruction, in this case generated through KBase (Arkin et al., 2018). Based
1279 on manually gathered experimental data, gap-filling solutions that had been manually
1280 determined in a subset of reconstructions are propagated by DEMETER to newly
1281 reconstructed strains. Moreover, DEMETER ensures correct reconstruction structure
1282 through use of a curated reaction and metabolite database and removes futile cycles
1283 resulting in unrealistically high ATP production. A test suite ensures agreement with the
1284 input experimental data and verifies model features such as mass and charge balance
1285 and feasible ATP production. The *Eggerthella lenta* DSM 2243 reconstruction

1286 underwent additional refinement of reactions and gene annotations against manually
1287 performed comparative genomics analyses (Heinken et al., 2020).

1288 Reconstructions were analyzed using the Cobra Toolbox version 3.0 (Heirendt et
1289 al., 2019) in Matlab version 2018b, with the IBM Cplex solver version 128. Defined
1290 media concentrations were mapped from compound names to BiGG metabolite IDs
1291 (King et al., 2016) and converted to cell uptake rates over the duration of *E. lenta*'s
1292 exponential growth phase in batch culture (**Table S1**) using the *concToCellRate*
1293 function in the Cobra Toolbox and an approximate cell dry weight of 3.3×10^{-13} g,
1294 calculated based on colony forming units and dry biomass quantification from two
1295 aliquots of a late-exponential phase EDM1 culture. Additional compounds detected in
1296 sterile culture media with high confidence based on untargeted metabolomics were
1297 included in the simulation media with a fixed maximum uptake rate of 1 mM/gDW/hr.

1298 The collection of *E. lenta* strain reconstructions included two reconstructions of
1299 the type strain: the DSM 2243 reconstruction which had undergone additional
1300 comparative genomics curation with PubSeed (Overbeek et al., 2014), and a slightly
1301 smaller and less refined reconstruction included in the AGORA2 collection (Heinken et
1302 al., 2020) based on genome resequencing of the ATCC 25559 version of the type
1303 strain. Neither reconstruction initially displayed nonzero growth in EDM1 using flux
1304 balance analysis. In order to facilitate interpretation of FBA results and avoid excess
1305 gap-filled reactions, we used the simpler *E. lenta* ATCC 25559 type strain
1306 reconstruction as the basis for subsequent curation and analysis. We transferred
1307 reactions present in the DSM 2243 reconstruction into this version if they were
1308 supported by genome annotations from other sources (Prokka (Seemann, 2014),
1309 GapMind (Price et al., 2022)) and/or by experimental growth or metabolomics data. We
1310 also performed several additional custom curations. Transporters were added for
1311 metabolites identified with high confidence (Metabolomics Standards Initiative level 1)
1312 and detected as secreted or depleted with a \log_2 fold change greater than 2 in the
1313 stationary phase strain collection metabolomics dataset (**Figure 4**). Several pathways
1314 were also modified based on growth assay results and/or pathway annotation software
1315 (Price et al., 2022) and (Pascal Andreu et al., 2021)). Curations were checked for viable
1316 growth in EDM1 using flux balance analysis. Reconstructions for the other 23 strains

1317 were only curated to ensure growth in EDM1 and to allow import/export based on
1318 metabolomics data, but not based on genome analysis with GapMind (Price et al.,
1319 2022) or the results of leave-one-out growth experiments, since those were only
1320 performed using the type strain. A complete summary of all curation steps is found in
1321 **Table S3**.

1322 Flux balance analysis (FBA), parsimonious flux balance analysis (pFBA), and flux
1323 variability analysis (FVA) were performed using the Cobra Toolbox functions
1324 *optimizeCbModel*, *minimizeModelFlux*, and *fastFVA*, respectively. Flux variability ranges
1325 are reported for 99% of the maximum growth rate.

1326 Metabolite uptake and secretion ranges estimated by FVA were compared with
1327 the stationary phase strain collection metabolomics dataset (shown in **Figure 4**). To
1328 compare metabolite data with FVA estimates, identified metabolites were first mapped
1329 from InChIKey metabolite IDs to KEGG IDs using the CTS Convert utility (Wohlgemuth
1330 et al., 2010) implemented in the R package *webchem* (Szöcs et al., 2020). KEGG IDs
1331 were then mapped to BiGG IDs using the BiGG database (King et al., 2016) and
1332 manually checked for consistency with compound IDs in the AGORA models. For
1333 purposes of this analysis, metabolites were considered produced if they had a \log_2 fold
1334 change greater than 0.5 in supernatants from at least one of the three type strain
1335 isolates included in the experiment (*E. lenta* DSM 2243 - UCSF, *E. lenta* ATCC 25559,
1336 and *E. lenta* DSM 2243 - DSMZ), and depleted if the \log_2 fold change was less than -
1337 0.5.

1338 To compare gene expression values with model flux estimates, we first ran pFBA
1339 and FVA for the modified EDM1 condition used for RNA-Seq (with 70% of the standard
1340 levels of arginine and acetate). We obtained the set of genes linked to reactions in the
1341 iEL2243_2 reconstruction, using NCBI BLASTn to map genes between different sets of
1342 annotations. Genes linked to multiple reactions were counted multiple times for each
1343 reaction, and vice versa. Only genes linked to reactions in the original ATCC 25559
1344 reconstruction were included.

1345 Similarly, to compare reaction knock-out predictions with strain variation, genes
1346 linked to reactions in the original ATCC 25559 reconstruction were mapped to
1347 annotations used in a previous pan-genome analysis of 31 non-clonal *E. lenta* genomes

1348 (Bisanz et al., 2020). In this previous analysis, amino acid sequence families were
1349 clustered across genomes using ProteinOrtho (Lechner et al., 2011) with cutoffs of 60%
1350 identity and 80% coverage. This analysis was then used to determine the number of
1351 strains in which each gene family in the ATCC 25559 reconstruction was present, and
1352 compare that distribution with the effects predicted by knockout analysis of the
1353 unconstrained model.

1354

1355 **Strain comparative metabolomics analysis**

1356 Metabolites were classified as strain-variably produced/depleted if they were
1357 differentially increased/decreased (FDR-adjusted $p < 0.1$ and absolute \log_2 fold
1358 change > 0.5) in supernatants from at least 1 isolate strain but fewer than 29 (of the 30
1359 isolates included in this experiment).

1360 The phylogenetic and comparative genomics analyses used in this study were
1361 previously reported, including a core gene phylogenetic tree (PhyloPhlan), gene family
1362 clustering across strains (ProteinOrtho) and Prokka and GhostKoala annotation of all
1363 genomes (Bisanz et al., 2020).

1364 Procrustes analysis was performed using the R package *vegan* v2.6-2, with
1365 evaluation of significance using the *protest* function (Oksanen et al., 2022). The *E.*
1366 *sinensis* isolate was excluded from Procrustes analysis to avoid skewing the distribution
1367 of phylogenetic distances.

1368 The gene-metabolite association analysis was performed as described previously
1369 (Bisanz et al., 2020), with different cutoffs for prioritization. Briefly, all observed patterns
1370 of gene family presence-absence (based on clusters of 60% identity and 80% coverage)
1371 were enumerated across the collection of genomes. Log-transformed metabolite
1372 intensities were then tested for association with each presence-absence pattern using
1373 Welch's t-tests. Using an initial cutoff of an FDR-adjusted p -value of 10^{-4} , 39.0% of
1374 metabolite features were significantly associated with a gene cluster by this method. To
1375 further restrict results to those features most likely to depend on the presence of a gene,
1376 we filtered gene-metabolite links using two additional separability criteria. First, the
1377 difference in median \log_{10} metabolite values between strain samples with and without
1378 the gene was required to be at least 0.4. Secondly, the 10th percentile \log_{10} metabolite

1379 value for strains with the gene was required to be at least 0.4 above the maximum value
1380 in controls, and the 90th percentile value for strains without the gene was required to be
1381 lower than that value. Finally, only the highest association for each metabolite feature
1382 was retained. This additional filtering resulted in the final table of 84 gene family-
1383 metabolite links. KEGG pathway enrichment analysis of the final gene set was
1384 performed using *clusterProfiler* v4.0.5 (Wu et al., 2021) with a *p*-value cutoff of 0.1.

1385

1386 **Cross-dataset untargeted metabolomics analysis**

1387 As described above, untargeted metabolomics datasets from supernatant,
1388 mouse intestinal contents, and serum were collected using the same chromatography
1389 and mass spectrometry methods. Pairs of features were compared across these
1390 datasets and linked if they were within 0.007 *m/z*, 0.5 minutes retention time, and had a
1391 cosine similarity of at least 0.205 between their MS2 spectra for positive ionization
1392 mode and 0.251 for negative ionization mode. Features for which MS2 spectra were not
1393 collected were linked to other features within 0.001 *m/z* and 0.2 retention time. Linked
1394 feature pairs were also required to be annotated as the same adduct. These *m/z* and
1395 retention time thresholds were chosen based on examination of the distributions of
1396 pairwise differences between features. The cosine similarity cutoffs were chosen as the
1397 99.5th percentile of cosine similarity between a large sample of unrelated feature pairs:
1398 specifically, all pairwise comparisons of two sets of 200 randomly sampled features with
1399 retention times differing by at least 1 and *m/z* differing by at least 0.01. This procedure
1400 was repeated separately for positive and negative ionization mode datasets. Under
1401 these criteria, only approximately 0.5% of linked features assigned an identity were
1402 linked to features with a conflicting identity. Linked pairs of features were merged into
1403 shared metabolite IDs that were carried forward for cross-dataset analysis and
1404 comparison.

1405

1406 **QUANTIFICATION AND STATISTICAL ANALYSIS**

1407 All statistical analyses were performed in R v4.1.1, with data visualizations
1408 generated using the *ggplot2* package (Wickham, 2016). Statistical tests, sample size
1409 and standard error are reported in the figures and figure legends. Benjamini-Hochberg

1410 false discovery rate (FDR) correction was used to adjust for multiple comparisons in all
1411 cases.

1412

1413 **Untargeted metabolomics statistical analysis**

1414 Differential trajectories across time series datasets were assessed using spline
1415 models implemented in the *santaR* package (Wolfer, 2022). Differential abundance
1416 analysis between supernatant samples and sterile controls at the final time point was
1417 performed using Welch's t-tests after checking assumptions of normality. In one case
1418 where cross-contamination of sterile control tubes occurred at later time points, features
1419 at those time points were compared with control samples from the last uncontaminated
1420 time point.

1421 Differential abundance analysis for the comparative strains dataset was
1422 performed using linear models with each strain identity as a covariate. Differential
1423 abundance analysis for the gnotobiotic mouse intestinal dataset was performed using
1424 linear mixed models with the R package *lmerTest* (Kuznetsova et al., 2017),
1425 incorporating fixed effects for intestinal site, colonization group, and the interaction
1426 between them; and nested random effects for cage and animal. The *diffIsmeans*
1427 function with Benjamini-Hochberg multiple hypothesis adjustment was used to evaluate
1428 the statistical significance of differences of each colonization group vs. germ-free under
1429 this model.

1430

1431 **Statistical analysis of growth curves**

1432 Growth curves were normalized based on average time-matched readings from
1433 blank control wells. Normalized values were used to fit logistic growth models for each
1434 well using the R package *growthcurver* (Sprouffske and Wagner, 2016). Low-quality
1435 model fits ($\sigma > 0.1$) were removed prior to calculation of summarized parameter
1436 values.

1437

1438 **Targeted metabolomics statistical analysis**

1439 Differential abundance analysis was performed using a linear model with terms
1440 for time point, strain, and their interaction. Differences from controls under the resulting

1441 model were estimated using Dunnett's method as implemented in the package
1442 *emmeans* v1.7.5 (Lenth, 2022).

1443

1444 **RNA-Seq statistical analysis**

1445 Differential expression analysis was performed using negative binomial
1446 generalized linear models implemented in the *DESeq2* package v1.32.0 (Love et al.,
1447 2014).

1448

1449

1450

1451 SUPPLEMENTAL INFORMATION TITLES AND LEGENDS

1452

1453 Supplemental Figures

1454 **Figure S1. EDM1 chemically defined media supports robust growth of *Eggerthella*** 1455 ***lenta* and enables sensitive metabolomics profiling. Related to Figure 1. A)**

1456 Summary of the composition of EDM1 media. The number in parentheses indicates the
1457 number of specific compounds in each category. **B)** Growth of *E. lenta* DSM 2243 in two
1458 commonly used media conditions (Brain Heart Infusion supplemented with L-arginine,
1459 and ISP-2 media supplemented with L-arginine), compared with three initial defined
1460 media formulations. **C)** Comparison of total number of differentially abundant features
1461 and identified differentially abundant features in this experiment compared to previous
1462 metabolomics profiling of *E. lenta*. The combination of chemically defined culture media
1463 and untargeted metabolomics methods used in this experiment allowed for greater
1464 detection of metabolites produced by *E. lenta*. **D)** Metabolomics profiling of compounds
1465 known to be present in the chemically defined media formulation EDM1. 22 media
1466 compounds were detected, most of which were not significantly depleted in *E. lenta*
1467 cultures over time. **E)** Hierarchical clustering of metabolite trajectories reveals distinct
1468 growth phases. Scaled average metabolite intensities across time points during growth
1469 in EDM1 were hierarchically clustered with complete linkage and cut into discrete
1470 clusters with a height of 1.6, distinguishing early-, mid- and late-produced and depleted
1471 metabolites. Cluster order is arbitrary. Annotated metabolites are listed below each
1472 cluster along with their Metabolomics Standards Initiative confidence level. Colors
1473 indicate ClassyFire metabolite classes as assigned by GNPS. Only clusters with at least
1474 1 identified metabolite and at least 5 total features are shown.

1475

1476 **Figure S2. Effects of individual media components on growth of *E. lenta* DSM** 1477 **2243. Related to Figure 1. A)** Growth curves for *E. lenta* DSM2243 growth in EDM1

1478 media with individual media components removed. Gray curves indicate growth in full
1479 EDM1 media in the same experiment. Curves are shown as mean +/- standard error.
1480 Blue text indicates the growth parameters with significantly different values with and
1481 without the compound (Wilcoxon rank-sum test, FDR-adjusted $p < 0.2$; r - growth rate k

1482 - carrying capacity, *tmid* - time to mid-exponential, *auc* - area under the empirical curve).
1483 **B)** Distribution of median effects of removal of all tested compounds on growth
1484 parameters estimated by a logistic model. The dotted line indicates the median
1485 parameter estimate for the full EDM1 media across all experiments. Parameters were
1486 fitted with a logistic model implemented by the R package *growthcurver*.

1487
1488 **Figure S3. Environmental acetate concentrations affect growth and metabolite**
1489 **production of three *E. lenta* strains. Related to Figure 2. A)** Targeted quantification
1490 of acetate depletion in *E. lenta* EDM1 cultures. Acetate was measured at 2-3 time points
1491 in supernatant samples from three *E. lenta* strains during growth in EDM1 as well as
1492 sterile controls. Quantification was performed using a method for derivatization of
1493 carboxylic acids with 3-nitrophenylhydrazine and N-(3-dimethylaminopropyl)-N'-
1494 ethylcarbodiimide followed by targeted LC-MS/MS. Error bars show mean +/- standard
1495 error. Linear models of acetate concentration versus strain and time point were inferred
1496 for each media group, and differences from controls under the resulting model were
1497 estimated using Dunnett's method. * indicates $p < 0.05$, *** indicates $p < 0.001$. **B)** Growth
1498 of three *E. lenta* strain isolates in EDM1 with 0, 1, or 10 mM sodium acetate. Mean +/-
1499 standard error across three replicates is shown. **C)** Acetate-responsive metabolites in
1500 supernatants from *E. lenta* AB8n2 and *E. lenta* Valencia. Metabolites shown are those
1501 that were assigned an identification, were differentially abundant compared with sterile
1502 controls (FDR-adjusted $p < 0.2$), and had significantly different trajectories over time in
1503 the presence vs absence of acetate in either strain (based on smoothing spline
1504 regression with the R package *santaR*, FDR-adjusted $p < 0.25$). Values shown are scaled
1505 log-transformed peak heights. The number in parentheses indicates the Metabolomics
1506 Standards Initiative confidence level for each metabolite annotation (see *Methods*).

1507
1508 **Figure S4. Consistent incorporation of acetate across three *E. lenta* strains based**
1509 **on stable isotope-resolved metabolomics. Related to Figure 2. A)** Growth of *E.*
1510 *lenta* strains in EDM1 with varying levels of sodium acetate (either stable isotope-
1511 labeled $^{13}\text{C}_2$ or unlabeled). Optical density measurements were taken and supernatant
1512 samples were collected at each indicated time point. Mean +/- standard error across

1513 three replicates is shown. **B)** Average trajectories of labeled extracellular metabolites in
1514 three different strains of *E. lenta*. Metabolites shown are those with $> 50\%$ and $> 5 \times 10^4$
1515 average peak area from labeled isotopologues in at least one time point in the 10 mM
1516 labeled acetate group. For metabolites detected in both positive and negative ionization
1517 mode, only positive mode is shown. The value in parentheses indicates the
1518 Metabolomics Standards Initiative annotation confidence level for each metabolite. **C)**
1519 Labeled metabolites of known identity in intracellular extracts across three strains of *E.*
1520 *lenta* (data for DSM 2243 matches [Figure 2E](#)). Each panel shows the average mass
1521 isotopologue distribution across three replicates for a single metabolite in intracellular
1522 extracts from time point 5 (39 hours, late exponential phase). Metabolites are labeled
1523 with the compound name and Metabolomics Standards Initiative annotation confidence
1524 level in parentheses. Metabolites included are those with $> 15\%$ and $> 10^4$ average
1525 peak area from labeled isotopologues in either the 1 mM or 10 mM labeled acetate
1526 group. *N*-acetylated amino acids are excluded for space and reported in [Data S1](#). The
1527 isotopologue color legend is the same as in panel B. **D)** Labeled metabolites of
1528 unknown identity across three strains of *E. lenta*. Each panel shows the average mass
1529 isotopologue distribution (across three replicates) for a single metabolite in intracellular
1530 extracts from time point 5 (39 hours, late exponential phase). Metabolites are labeled
1531 with their estimated exact mass, retention time, and ionization mode. Metabolites
1532 included are those with $> 15\%$ and $> 10^4$ average peak area from labeled isotopologues
1533 in either the 1 mM or 10 mM labeled acetate group. The isotopologue color legend is
1534 the same as in panels B and C.

1535
1536 **Figure S5. Stable isotope profiling of *E. lenta* arginine metabolism confirms that**
1537 **arginine is primarily converted to ornithine as an energy source. Related to**
1538 **Figure 2. A)** Citrulline, but not ornithine, has a similar effect as L-arginine on *E. lenta*
1539 growth. Growth curves of *E. lenta* grown in EDM1 media where the 1% L-arginine (red)
1540 has been replaced with an equimolar quantity of either L-citrulline (blue) or L-ornithine
1541 (green). Curves show mean \pm standard error across four replicates. **B)** In *E. lenta*
1542 DSM 2243 cultures grown with 1% $^{13}\text{C}_6$ labeled arginine, correspondingly labeled
1543 citrulline and ornithine accumulate in supernatants over the course of growth. Curves

1544 show mean +/- standard error across three replicates. **C)** Mass isotopologue
1545 distributions of extracellular metabolites. Each barplot shows the isotopologue mean
1546 peak areas for each feature over time. Compounds shown are those of known identity
1547 that increase by a factor of at least 2^4 , have at least one isotopologue with a peak area
1548 of greater 10^6 in at least one time point, and have a labeled isotopologue with >3%
1549 abundance in at least one time point. **D)** Mass isotopologue distributions of intracellular
1550 metabolites. Each barplot shows the mean peak areas of isotopologues for each feature
1551 at two time points. Compounds shown are those of known identity with an average
1552 labeled MID > 0.1 and a total peak area from labeled isotopologues of at least 10^5 in at
1553 least one time point. The isotopologue color legend is the same as in panel C. **E)**
1554 Distribution of total signal of extracellular metabolites across labeling patterns. While
1555 signal from numerous unlabeled compounds is detected over time (left panel),
1556 compounds with M+5 labeling patterns are mainly restricted to ornithine, citrulline, and a
1557 compound of unknown identity (middle panel), and compounds found with high signal
1558 as M+6 isotopologues are mainly arginine and citrulline (right-hand panel). Compounds
1559 shown are those with the highest peak areas at the final time point in positive ionization
1560 mode. **F)** Hypothesized pathways for metabolism of L-arginine by *E. lenta*. Circles
1561 indicate the number of carbon atoms in selected compounds and are colored blue to
1562 indicate incorporation of ^{13}C isotopes from external arginine. Compound names in bold
1563 were detected with the observed labeling patterns in either intracellular metabolite
1564 extracts or culture supernatants.

1565
1566 **Figure S6. Single-reaction knockout analysis of iEL2243_2 identifies conserved**
1567 **genes across metabolic subsystems. Related to Figure 3. A)** Predicted effects of
1568 knocking out reactions in the top 20 largest subsystems on growth of *E. lenta*, according
1569 to pFBA analysis of the iEL2243_2 model. Reactions designated “Has effect” are those
1570 for which the knockout has a predicted maximum growth rate less than wild-type but
1571 greater than 0. Essential reactions are those that reduced biomass flux to 0 when
1572 removed from the model. **B)** Reactions linked to more conserved gene families are
1573 more likely to have substantial effects on growth when removed. Each point represents
1574 a reaction, separated on the x-axis by whether the model without that reaction grew at >

1575 70% of the wildtype model. The y-axis indicates the fraction of *E. lenta* strain genomes
1576 in which gene families (defined using ProteinOrtho clustering) linked to that reaction
1577 were present.

1578

1579 **Figure S7. Within-species variation in *E. lenta* metabolic profiles across genomes**
1580 **and metabolomes. Related to Figure 4. A)** Phylogeny of 30 *Eggerthella* strains
1581 analyzed in this study. This phylogeny was previously constructed based on core gene
1582 alignments using PhyloPhlan (Bisanz et al., 2020). **B)** Principal components analysis
1583 (PCA) of log-transformed metabolite intensity profiles of stationary phase supernatants
1584 from 30 *Eggerthella* isolates in EDM1. The right panel shows the largest feature
1585 loadings for the PCA and their corresponding chemical classes as assigned by GNPS,
1586 where available. Dereplicated metabolite features with an average value $> 10^5$ in at
1587 least one strain were included. **C)** Distribution of the number of strains producing or
1588 depleting each metabolite feature. Features included are those that were significantly
1589 modified by at least one *Eggerthella* isolate in this experiment (FDR-adjusted p -
1590 value < 0.1 and \log_2 fold change > 0.5). **D)** Map of the teichoic acid biosynthesis region of
1591 the genome of representative *Eggerthella* strains. Genes outlined in bold are the gene
1592 families associated with the unidentified metabolite features shown in [Figure 4E](#). Gene
1593 regions were defined in each genome based on the location of the genes annotated as
1594 *tagG* and *tagH* by Prokka. **E)** Distribution of core and accessory reactions across
1595 subsystems, based on comparative analysis of metabolic reconstructions of 24 *E. lenta*
1596 strain genomes. **F)** Predicted maximum growth rate inferred by flux balance analysis of
1597 each of the 24 *E. lenta* strain reconstructions in 52 leave-one-out media conditions
1598 based on EDM1. Gray tiles indicate predicted cases of zero growth.

1599

1600 **Figure S8. Differential abundance analysis of intestinal and serum metabolites of**
1601 ***E. lenta*-monocolonized mice compared to germ-free. Related to Figure 5. A)**
1602 Volcano plots of differential abundance analysis of metabolite features in intestinal
1603 contents and serum of gnotobiotic mice monocolonized with one of three *E. lenta*
1604 strains. Effect sizes and significance are estimated from group comparisons based on
1605 linear mixed models of log-transformed metabolite abundances, accounting for animal

1606 and cage random effects. **B)** Total number of untargeted metabolomics features in
1607 intestinal contents and serum of gnotobiotic mice that could be linked to features in
1608 either of two *in vitro* EDM1 metabolomics datasets, based on high similarity of *m/z*,
1609 retention time, and MS2 spectra. **C)** Comparison of the effect of *E. lenta* DSM 2243 on
1610 metabolites detected in both EDM1 cultures in the untargeted time course experiment
1611 and monoclonized mice. Each point represents a metabolite feature detected in both
1612 datasets. The x-axis indicates the log₂ fold change of each feature in supernatants from
1613 the *E. lenta* DSM 2243 time course experiment compared with sterile controls,
1614 compared with the covariate-adjusted log₂ fold change of that feature in monoclonized
1615 mice compared with germ-free mice. Points are colored green if the feature is
1616 significantly differentially abundant in gnotobiotic mice and is shifted in the same
1617 direction by the corresponding strain in the time course *in vitro* experiment.

1618

1619 **Figure S9. Shifts in intestinal amino acid metabolites of *E. lenta*-monocolonized**
1620 **mice compared to germ-free. Related to Figure 6. A)** Annotated metabolites with the
1621 largest shifts in intestinal contents of *E. lenta*-colonized mice compared with germ-free.
1622 Metabolites are shown if they were identified based on library comparison and were
1623 among the most 600 strongly shifted features in any individual site or colonization
1624 group, based on linear mixed models. Each point shows the effect size in a single site,
1625 and color indicates chemical class where available (assigned using feature-based
1626 molecular networking with GNPS). **B)** Abundance of arginine and agmatine-related
1627 metabolites in gnotobiotic mice. Arginine is only slightly depleted by *E. lenta*, although
1628 its expected products, ornithine and citrulline, are greatly increased. Agmatine is
1629 significantly depleted, while its expected product, putrescine, is not significantly
1630 increased. ‘.’ indicates Benjamini-Hochberg adjusted $p < 0.1$, * $p < 0.05$, ** $p < 0.01$,
1631 *** $p < 0.001$. **C)** Volcano plots illustrating shifts in the abundance of proteinogenic amino
1632 acids in *E. lenta*-colonized mice. Arginine is colored in green. Effect sizes and
1633 significance are estimated from group comparisons based on linear mixed models of
1634 log-transformed metabolite abundances, accounting for animal and cage random
1635 effects.

1636

1637 **Supplemental Tables**

1638

1639 **Table S1. Chemically defined media formulations used in this study. Related to**
1640 **Figure 1 and STAR Methods.** Recipes used for preparation of chemically defined
1641 media used for experiments in this study. The first two columns indicate the
1642 manufacturer information for each compound and the concentration of working solution
1643 prepared for that compound. Unless otherwise specified, reference to EDM1 indicates
1644 that the “Standard EDM1” preparation was used.

1645

1646 **Table S2. Summarized results of media leave-one-out growth experiments.**
1647 **Related to Figure 1.** Parameters were fit by logistic growth models using the R
1648 package *growthcurver*. A separate model was fit for each replicate in each experiment,
1649 and the average and standard deviation for each parameter across replicates are
1650 reported. Average growth rate r was calculated as a harmonic mean.

1651

1652 **Table S3. Curation steps applied to *E. lenta* DSM 2243 AGORA reconstruction.**
1653 **Related to Figure 3.** Summary of curation steps, supporting data, and gene
1654 annotations for each reaction added or modified in the iEL2243_2 reconstruction.

1655

1656 **Table S4. Most highly expressed genes by *E. lenta* DSM 2243 during growth in**
1657 **EDM1. Related to Figure 3.** Locus tags, gene annotation, and average and standard
1658 deviation of the 100 most highly expressed transcripts during *E. lenta* growth in the
1659 baseline EDM1 condition.

1660

1661 **Table S5. Metabolite features associated with variable *E. lenta* gene families**
1662 **across strains. Related to Figure 4.** Results of association analysis linking patterns of
1663 strain-variable genes with strain-variable metabolite features. Associations listed are
1664 those that met the strictest significance and separability criteria (see *Methods*). Gene
1665 annotations are listed for association patterns with 20 or fewer candidate gene families.

1666

1667 **Table S6. Summary of conserved and strain-variable reactions by subsystem in *E.***
1668 ***lenta* strain metabolic reconstructions. Related to Figure 4.** Statistics on the
1669 distribution of core and accessory reactions across *E. lenta* strain metabolic
1670 reconstructions.

1671
1672 **Table S7. Genes linked to agmatine utilization by *E. lenta*. Related to Figure 6. A)**
1673 KEGG annotations of gene families in the agmatine deiminase pathway in *E. lenta*
1674 genomes, as previously obtained using GhostKoala. **B)** *E. lenta* DSM 2243 genes with
1675 differential expression in response to agmatine sulfate treatment (FDR-adjusted $p < 0.1$
1676 and absolute log₂ fold change > 1), as estimated by DESeq2.

1677
1678 **Table S8. Supplementary oligonucleotide probes used for depletion of highly**
1679 **abundant *E. lenta* noncoding RNAs. Related to STAR Methods.** Probes designed
1680 for depletion of *E. lenta* ribosomal RNA and highly abundant *ssrA* and *rnpB* noncoding
1681 RNAs, used in Illumina Ribo-Zero library preparation.

1682 1683 **Supplemental Datasets**

1684
1685 **Data S1. Labeled features detected in stable isotope experiments. Related to**
1686 **Figure 2.** Summary of labeled isotopologues detected by untargeted metabolomics.
1687 Each tab includes data for a single experiment and sample type: extracellular
1688 metabolites with labeled acetate, intracellular metabolites with labeled acetate,
1689 extracellular metabolites with labeled arginine, and intracellular metabolites with labeled
1690 arginine. In addition to basic properties of each compound/feature, the average peak
1691 area, standard error in peak area, and average fractional distribution are reported for
1692 each detected isotopologue. Compounds were filtered based on the same criteria as in
1693 **Figures 2, S6, and S7.**

1694
1695 **Data S2. Differentially abundant features across *in vivo* and *in vitro* untargeted**
1696 **metabolomics datasets. Related to Figure 5.** Each tab lists the set of untargeted
1697 metabolomics features that were differentially abundant (linear mixed effects models,

1698 absolute \log_2 fold change estimate > 1 and FDR-adjusted p -value < 0.2) in at least at
1699 least one intestinal site between *E. lenta*-colonized and GF mice, and that were also
1700 detected in *in vitro* untargeted metabolomics experiments, separated by strain and by
1701 feature annotation status (identified/unknown). For each feature, the corresponding \log_2
1702 fold change and significance in the *in vitro* dataset(s) are listed for comparison.
1703 Features are ordered by their effect size in cecal contents.

1704 REFERENCES

- 1705 Alexander, M., Ang, Q.Y., Nayak, R.R., Bustion, A.E., Sandy, M., Zhang, B., Upadhyay,
1706 V., Pollard, K.S., Lynch, S.V., and Turnbaugh, P.J. (2021). Human gut bacterial
1707 metabolism drives Th17 activation and colitis. *Cell Host Microbe* 0.
1708 <https://doi.org/10.1016/j.chom.2021.11.001>.
- 1709 Almeida, A., Mitchell, A.L., Boland, M., Forster, S.C., Gloor, G.B., Tarkowska, A.,
1710 Lawley, T.D., and Finn, R.D. (2019). A new genomic blueprint of the human gut
1711 microbiota. *Nature* <https://doi.org/10.1038/s41586-019-0965-1>.
- 1712 Amador-Noguez, D., Feng, X.-J., Fan, J., Roquet, N., Rabitz, H., and Rabinowitz, J.D.
1713 (2010). Systems-level metabolic flux profiling elucidates a complete, bifurcated
1714 tricarboxylic acid cycle in *Clostridium acetobutylicum*. *J. Bacteriol.* 192, 4452–4461.
- 1715 Arkin, A.P., Cottingham, R.W., Henry, C.S., Harris, N.L., Stevens, R.L., Maslov, S.,
1716 Dehal, P., Ware, D., Perez, F., Canon, S., et al. (2018). KBase: The United States
1717 Department of Energy Systems Biology Knowledgebase. *Nat. Biotechnol.* 36, 566–569.
- 1718 Beloborodov, N.V., Khodakova, A.S., Bairamov, I.T., and Olenin, A.Y. (2009). Microbial
1719 origin of phenylcarboxylic acids in the human body. *Biochemistry* 74, 1350–1355.
- 1720 Bess, E.N., Bisanz, J.E., Yarza, F., Bustion, A., Rich, B.E., Li, X., Kitamura, S.,
1721 Waligurski, E., Ang, Q.Y., Alba, D.L., et al. (2020). Genetic basis for the cooperative
1722 bioactivation of plant lignans by *Eggerthella lenta* and other human gut bacteria. *Nat*
1723 *Microbiol* 5, 56–66.
- 1724 Bisanz, J.E., Soto-Perez, P., Noecker, C., Aksenov, A.A., Lam, K.N., Kenney, G.E.,
1725 Bess, E.N., Haiser, H.J., Kyaw, T.S., Yu, F.B., et al. (2020). A Genomic Toolkit for the
1726 Mechanistic Dissection of Intractable Human Gut Bacteria. *Cell Host Microbe* 1–14.
- 1727 Brown, S., Santa Maria, J.P., Jr, and Walker, S. (2013). Wall teichoic acids of gram-
1728 positive bacteria. *Annu. Rev. Microbiol.* 67, 313–336.
- 1729 Buttimer, C., Bottacini, F., Shkoporov, A.N., Draper, L.A., Ross, P., and Hill, C. (2022).
1730 Selective Isolation of *Eggerthella lenta* from Human Faeces and Characterisation of the
1731 Species Prophage Diversity. *Microorganisms* 10, 195.
- 1732 Cekanaviciute, E., Yoo, B.B., Runia, T.F., Debelius, J.W., Singh, S., Nelson, C.A.,
1733 Kanner, R., Bencosme, Y., Lee, Y.K., Hauser, S.L., et al. (2017). Gut bacteria from
1734 multiple sclerosis patients modulate human T cells and exacerbate symptoms in mouse
1735 models. *Proc. Natl. Acad. Sci. U. S. A.* 114, 10713–10718.
- 1736 Chen, J., Wright, K., Davis, J.M., Jeraldo, P., Marietta, E.V., Murray, J., Nelson, H.,
1737 Matteson, E.L., and Taneja, V. (2016). An expansion of rare lineage intestinal microbes
1738 characterizes rheumatoid arthritis. *Genome Med.* 8, 43.

- 1739 Chen, S., Zhou, Y., Chen, Y., and Gu, J. (2018). fastp: an ultra-fast all-in-one FASTQ
1740 preprocessor. *Bioinformatics* 34, i884–i890.
- 1741 Chiu, H.-C., Levy, R., and Borenstein, E. (2014). Emergent Biosynthetic Capacity in
1742 Simple Microbial Communities. *PLoS Comput. Biol.* 10, e1003695.
- 1743 Chodkowski, J.L., and Shade, A. (2020). Exometabolite Dynamics over Stationary
1744 Phase Reveal Strain-Specific Responses. *mSystems* 5, e00493–20.
- 1745 de Crécy-Lagard, V., El Yacoubi, B., de la Garza, R.D., Noiriél, A., and Hanson, A.D.
1746 (2007). Comparative genomics of bacterial and plant folate synthesis and salvage:
1747 predictions and validations. *BMC Genomics* 8, 245.
- 1748 van Dalen, R., Peschel, A., and van Sorge, N.M. (2020). Wall Teichoic Acid in
1749 *Staphylococcus aureus* Host Interaction. *Trends Microbiol.* 28, 985–998.
- 1750 DeFelice, B.C., Mehta, S.S., Samra, S., Čajka, T., Wancewicz, B., Fahrman, J.F., and
1751 Fiehn, O. (2017). Mass Spectral Feature List Optimizer (MS-FLO): A tool to minimize
1752 false positive peak reports in untargeted liquid chromatography-mass spectroscopy (LC-
1753 MS) data processing. *Anal. Chem.* 89, 3250–3255.
- 1754 Devlin, A.S., and Fischbach, M.A. (2015). A biosynthetic pathway for a prominent class
1755 of microbiota-derived bile acids. *Nat. Chem. Biol.* 11, 685–690.
- 1756 Diener, C., Gibbons, S.M., and Resendis-Antonio, O. (2020). MICOM: Metagenome-
1757 Scale Modeling To Infer Metabolic Interactions in the Gut Microbiota. *mSystems* 5,
1758 e00606–e00619, [/mSystems/5/1/mSys.00606–00619.atom](https://doi.org/10.1128/mSystems.00606-20).
- 1759 Djoumbou Feunang, Y., Eisner, R., Knox, C., Chepelev, L., Hastings, J., Owen, G.,
1760 Fahy, E., Steinbeck, C., Subramanian, S., Bolton, E., et al. (2016). ClassyFire:
1761 automated chemical classification with a comprehensive, computable taxonomy. *J.*
1762 *Cheminform.* 8, 61.
- 1763 Duncan, S.H., Barcenilla, A., Stewart, C.S., Pryde, S.E., and Flint, H.J. (2002). Acetate
1764 Utilization and Butyryl Coenzyme A (CoA):Acetate-CoA Transferase in Butyrate-
1765 Producing Bacteria from the Human Large Intestine. *Appl. Environ. Microbiol.* 68, 5186–
1766 5190.
- 1767 Dunphy, L.J., Grimes, K.L., Wase, N., Kolling, G.L., and Papin, J.A. (2021). Untargeted
1768 Metabolomics Reveals Species-Specific Metabolite Production and Shared Nutrient
1769 Consumption by *Pseudomonas aeruginosa* and *Staphylococcus aureus*. *mSystems* 6.
1770 <https://doi.org/10.1128/mSystems.00480-21>.
- 1771 Ernst, M., Kang, K.B., Caraballo-Rodríguez, A.M., Nothias, L.-F., Wandy, J., Chen, C.,
1772 Wang, M., Rogers, S., Medema, M.H., Dorrestein, P.C., et al. (2019). MolNetEnhancer:
1773 Enhanced Molecular Networks by Integrating Metabolome Mining and Annotation Tools.
1774 *Metabolites* 9. <https://doi.org/10.3390/metabo9070144>.

- 1775 Fiehn, O., Robertson, D., Griffin, J., and van der Werf, M. (2007). The metabolomics
1776 standards initiative (MSI). *Metabolomics*.
- 1777 Franzosa, E.A., Sirota-Madi, A., Avila-Pacheco, J., Fornelos, N., Haiser, H.J., Reinker,
1778 S., Vatanen, T., Hall, A.B., Mallick, H., McIver, L.J., et al. (2018). Gut microbiome
1779 structure and metabolic activity in inflammatory bowel disease. *Nature Microbiology*
1780 <https://doi.org/10.1038/s41564-018-0306-4>.
- 1781 Galgano, F., Caruso, M., Condelli, N., and Favati, F. (2012). Focused review: agmatine
1782 in fermented foods. *Front. Microbiol.* 3, 199.
- 1783 Gardiner, B.J., Tai, A.Y., Kotsanas, D., Francis, M.J., Roberts, S.A., Ballard, S.A.,
1784 Junckerstorff, R.K., and Korman, T.M. (2015). Clinical and Microbiological
1785 Characteristics of *Enterthella lenta* Bacteremia. *J. Clin. Microbiol.* 53, 626–635.
- 1786 Girinathan, B.P., DiBenedetto, N., Worley, J.N., Peltier, J., Arrieta-Ortiz, M.L.,
1787 Immanuel, S.R.C., Lavin, R., Delaney, M.L., Cummins, C.K., Hoffman, M., et al. (2021).
1788 In vivo commensal control of *Clostridioides difficile* virulence. *Cell Host Microbe* 29,
1789 1693–1708.e7.
- 1790 Gu, C., Kim, G.B., Kim, W.J., Kim, H.U., and Lee, S.Y. (2019). Current status and
1791 applications of genome-scale metabolic models. *Genome Biol.* 20, 121.
- 1792 Gu, Z., Eils, R., and Schlesner, M. (2016). Complex heatmaps reveal patterns and
1793 correlations in multidimensional genomic data. *Bioinformatics* 32, 2847–2849.
- 1794 Haenisch, B., von Kugelgen, I., Bönisch, H., Göthert, M., Sauerbruch, T., Schepke, M.,
1795 Marklein, G., Höfling, K., Schröder, D., and Molderings, G.J. (2008). Regulatory
1796 mechanisms underlying agmatine homeostasis in humans. *Am. J. Physiol. Gastrointest.*
1797 *Liver Physiol.* 295, G1104–G1110.
- 1798 Haiser, H.J., Gootenberg, D.B., Chatman, K., Sirasani, G., Balskus, E.P., and
1799 Turnbaugh, P.J. (2013). Predicting and Manipulating Cardiac Drug Inactivation by the
1800 Human Gut Bacterium *Enterthella lenta*. *Science* 341, 295–298.
- 1801 Han, S., Van Treuren, W., Fischer, C.R., Merrill, B.D., DeFelice, B.C., Sanchez, J.M.,
1802 Higginbottom, S.K., Guthrie, L., Fall, L.A., Dodd, D., et al. (2021). A metabolomics
1803 pipeline for the mechanistic interrogation of the gut microbiome. *Nature* 595, 415–420.
- 1804 Harris, S.C., Devendran, S., Méndez- García, C., Mythen, S.M., Wright, C.L., Fields,
1805 C.J., Hernandez, A.G., Cann, I., Hylemon, P.B., and Ridlon, J.M. (2018). Bile acid
1806 oxidation by *Enterthella lenta* strains C592 and DSM 2243^T. *Gut Microbes* 1–17.
- 1807 van der Hee, B., and Wells, J.M. (2021). Microbial Regulation of Host Physiology by
1808 Short-chain Fatty Acids. *Trends Microbiol.* 29, 700–712.
- 1809 Heinken, A., Acharya, G., Ravcheev, D.A., Hertel, J., Nyga, M., Okpala, O.E., Hogan,
1810 M., Magnúsdóttir, S., Martinelli, F., Preciat, G., et al. (2020). AGORA2: Large scale

- 1811 reconstruction of the microbiome highlights wide-spread drug-metabolising capacities
1812 (Systems Biology).
- 1813 Heinken, A., Basile, A., and Thiele, I. (2021a). Advances in constraint-based modelling
1814 of microbial communities. *Current Opinion in Systems Biology* 27, 100346.
- 1815 Heinken, A., Magnúsdóttir, S., Fleming, R.M.T., and Thiele, I. (2021b). DEMETER:
1816 efficient simultaneous curation of genome-scale reconstructions guided by experimental
1817 data and refined gene annotations. *Bioinformatics* ttab622.
- 1818 Heirendt, L., Arreckx, S., Pfau, T., Mendoza, S.N., Richelle, A., Heinken, A.,
1819 Haraldsdóttir, H.S., Wachowiak, J., Keating, S.M., Vlasov, V., et al. (2019). Creation and
1820 analysis of biochemical constraint-based models using the COBRA Toolbox v.3.0. *Nat.*
1821 *Protoc.* 14, 639–702.
- 1822 Henry, C.S., DeJongh, M., Best, A.A., Frybarger, P.M., Linsay, B., and Stevens, R.L.
1823 (2010). High-throughput generation, optimization and analysis of genome-scale
1824 metabolic models. *Nat. Biotechnol.* 28, 977–982.
- 1825 Hertel, J., Harms, A.C., Heinken, A., Baldini, F., Thinner, C.C., Glaab, E., Vasco, D.A.,
1826 Pietzner, M., Stewart, I.D., Wareham, N.J., et al. (2019). Integrated Analyses of
1827 Microbiome and Longitudinal Metabolome Data Reveal Microbial-Host Interactions on
1828 Sulfur Metabolism in Parkinson’s Disease. *Cell Rep.* 29, 1767–1777.e8.
- 1829 Huynen, M.A., Dandekar, T., and Bork, P. (1999). Variation and evolution of the citric-
1830 acid cycle: a genomic perspective. *Trends Microbiol.* 7, 281–291.
- 1831 Hylemon, P.B., Harris, S.C., and Ridlon, J.M. (2018). Metabolism of hydrogen gases
1832 and bile acids in the gut microbiome. *FEBS Lett.* 592, 2070–2082.
- 1833 Islam, M.Z., Tran, M., Xu, T., Tierney, B.T., Patel, C., and Kostic, A.D. (2021).
1834 Reproducible and Opposing Microbiome Signatures Distinguish Autoimmune Diseases
1835 and Cancers: A Systematic Review and Meta-Analysis (In Review).
- 1836 Kim, D., Paggi, J.M., Park, C., Bennett, C., and Salzberg, S.L. (2019). Graph-based
1837 genome alignment and genotyping with HISAT2 and HISAT-genotype. *Nat. Biotechnol.*
1838 37, 907–915.
- 1839 King, Z.A., Lu, J., Dräger, A., Miller, P., Federowicz, S., Lerman, J.A., Ebrahim, A.,
1840 Palsson, B.O., and Lewis, N.E. (2016). BiGG Models: A platform for integrating,
1841 standardizing and sharing genome-scale models. *Nucleic Acids Res.* 44, D515–D522.
- 1842 Koppel, N., Bisanz, J.E., Pandelia, M.-E., Turnbaugh, P.J., and Balskus, E.P. (2018).
1843 Discovery and characterization of a prevalent human gut bacterial enzyme sufficient for
1844 the inactivation of a family of plant toxins. *Elife* 7, e33953.
- 1845 Koropatkin, N.M., Cameron, E.A., and Martens, E.C. (2012). How glycan metabolism
1846 shapes the human gut microbiota. *Nat. Rev. Microbiol.* 10, 323–335.

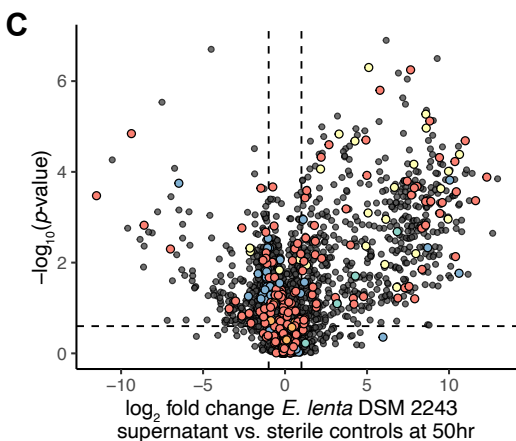
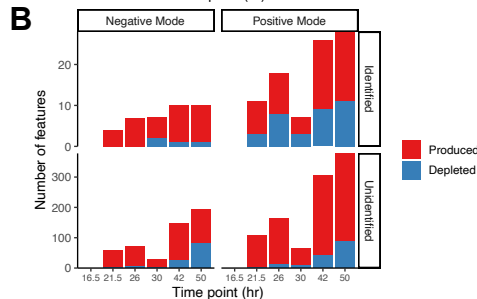
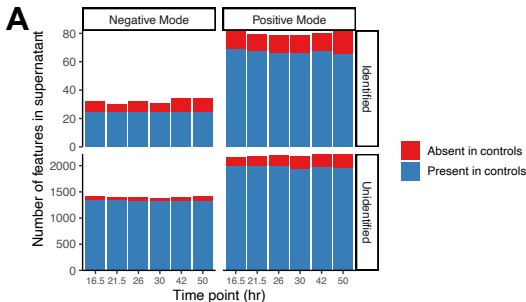
- 1847 Kuznetsova, A., Brockhoff, P.B., and Christensen, R.H.B. (2017). ImerTest Package:
1848 Tests in Linear Mixed Effects Models. *J. Stat. Softw.* *82*, 1–26.
- 1849 Lagkouvardos, I., Overmann, J., and Clavel, T. (2017). Cultured microbes represent a
1850 substantial fraction of the human and mouse gut microbiota. *Gut Microbes* *8*, 493–503.
- 1851 Lechner, M., Findeiß, S., Steiner, L., Marz, M., Stadler, P.F., and Prohaska, S.J. (2011).
1852 Proteinortho: Detection of (Co-)orthologs in large-scale analysis. *BMC Bioinformatics*
1853 *12*, 124.
- 1854 Lenth, R.V. (2022). emmeans: Estimated Marginal Means, aka Least-Squares Means.
- 1855 Levin, I., Giladi, M., Altman-Price, N., Ortenberg, R., and Mevarech, M. (2004). An
1856 alternative pathway for reduced folate biosynthesis in bacteria and halophilic archaea.
1857 *Mol. Microbiol.* *54*, 1307–1318.
- 1858 Li, D., Feng, Y., Tian, M., Ji, J., Hu, X., and Chen, F. (2021). Gut microbiota-derived
1859 inosine from dietary barley leaf supplementation attenuates colitis through PPAR γ
1860 signaling activation. *Microbiome* *9*, 83.
- 1861 Liao, Y., Smyth, G.K., and Shi, W. (2019). The R package Rsubread is easier, faster,
1862 cheaper and better for alignment and quantification of RNA sequencing reads. *Nucleic*
1863 *Acids Res.* *47*, e47.
- 1864 Liu, Y., Chen, H., Van Treuren, W., Hou, B.-H., Higginbottom, S.K., and Dodd, D.
1865 (2022). *Clostridium sporogenes* uses reductive Stickland metabolism in the gut to
1866 generate ATP and produce circulating metabolites. *Nat Microbiol* *7*, 695–706.
- 1867 Llácer, J.L., Polo, L.M., Tavárez, S., Alarcón, B., Hilario, R., and Rubio, V. (2007). The
1868 Gene Cluster for Agmatine Catabolism of *Enterococcus faecalis*: Study of Recombinant
1869 Putrescine Transcarbamylase and Agmatine Deiminase and a Snapshot of Agmatine
1870 Deiminase Catalyzing Its Reaction. *Journal of Bacteriology* *189*, 1254–1265.
1871 <https://doi.org/10.1128/jb.01216-06>.
- 1872 Love, M.I., Huber, W., and Anders, S. (2014). Moderated estimation of fold change and
1873 dispersion for RNA-seq data with DESeq2. *Genome Biol.* *15*.
1874 <https://doi.org/10.1186/s13059-014-0550-8>.
- 1875 Mager, L.F., Burkhard, R., Pett, N., Cooke, N.C.A., Brown, K., Ramay, H., Paik, S.,
1876 Stagg, J., Groves, R.A., Gallo, M., et al. (2020). Microbiome-derived inosine modulates
1877 response to checkpoint inhibitor immunotherapy. *Science* eabc3421.
- 1878 Maini Rekdal, V., Bess, E.N., Bisanz, J.E., Turnbaugh, P.J., and Balskus, E.P. (2019).
1879 Discovery and inhibition of an interspecies gut bacterial pathway for Levodopa
1880 metabolism. *Science* *364*, eaau6323.
- 1881 Maini Rekdal, V., Nol Bernadino, P., Luescher, M.U., Kiamehr, S., Le, C., Bisanz, J.E.,
1882 Turnbaugh, P.J., Bess, E.N., and Balskus, E.P. (2020). A widely distributed

- 1883 metalloenzyme class enables gut microbial metabolism of host- and diet-derived
1884 catechols. *Elife* 9. <https://doi.org/10.7554/eLife.50845>.
- 1885 Massengo-Tiassé, R.P., and Cronan, J.E. (2009). Diversity in enoyl-acyl carrier protein
1886 reductases. *Cell. Mol. Life Sci.* 66, 1507–1517.
- 1887 Medlock, G.L., Carey, M.A., McDuffie, D.G., Mundy, M.B., Giallourou, N., Swann, J.R.,
1888 Kolling, G.L., and Papin, J.A. (2018). Inferring Metabolic Mechanisms of Interaction
1889 within a Defined Gut Microbiota. *Cell Systems* 7, 245–257.e7.
- 1890 Molderings, G.J., Kribben, B., Heinen, A., Schröder, D., Brüß, M., and Göthert, M.
1891 (2004). Intestinal tumor and agmatine (decarboxylated arginine): low content in colon
1892 carcinoma tissue specimens and inhibitory effect on tumor cell proliferation in vitro.
1893 *Cancer* 101, 858–868.
- 1894 Monk, J.M., Charusanti, P., Aziz, R.K., Lerman, J.A., Premyodhin, N., Orth, J.D., Feist,
1895 A.M., and Palsson, B.O. (2013). Genome-scale metabolic reconstructions of multiple
1896 *Escherichia coli* strains highlight strain-specific adaptations to nutritional environments.
1897 *Proceedings of the National Academy of Sciences* 110, 20338–20343.
- 1898 Monk, J.M., Lloyd, C.J., Brunk, E., Mih, N., Sastry, A., King, Z., Takeuchi, R., Nomura,
1899 W., Zhang, Z., Mori, H., et al. (2017). iML1515, a knowledgebase that computes
1900 *Escherichia coli* traits. *Nat. Biotechnol.* 35, 904–908.
- 1901 Muñoz-Tamayo, R., Laroche, B., Walter, E., Doré, J., Duncan, S.H., Flint, H.J., and
1902 Leclerc, M. (2011). Kinetic modelling of lactate utilization and butyrate production by key
1903 human colonic bacterial species. *FEMS Microbiol. Ecol.* 76, 615–624.
- 1904 Noronha, A., Modamio, J., Jarosz, Y., Guerard, E., Sompairac, N., Preciat, G.,
1905 Daniëlsdóttir, A.D., Krecke, M., Merten, D., Haraldsdóttir, H.S., et al. (2018). The Virtual
1906 Metabolic Human database: integrating human and gut microbiome metabolism with
1907 nutrition and disease. *Nucleic Acids Res.* gky992–gky992.
- 1908 Nothias, L.-F., Petras, D., Schmid, R., Dührkop, K., Rainer, J., Sarvepalli, A., Protsyuk,
1909 I., Ernst, M., Tsugawa, H., Fleischauer, M., et al. (2020). Feature-based molecular
1910 networking in the GNPS analysis environment. *Nat. Methods* 17, 905–908.
- 1911 Oksanen, J., Simpson, G.L., Blanchet, F.G., Kindt, R., Legendre, P., Minchin, P.R.,
1912 O’Hara, R.B., Solymos, P., Stevens, M.H.H., Szoecs, E., et al. (2022). *vegan*:
1913 *Community Ecology Package*.
- 1914 Overbeek, R., Olson, R., Pusch, G.D., Olsen, G.J., Davis, J.J., Disz, T., Edwards, R.A.,
1915 Gerdes, S., Parrello, B., Shukla, M., et al. (2014). The SEED and the Rapid Annotation
1916 of microbial genomes using Subsystems Technology (RAST). *Nucleic Acids Res.* 42,
1917 D206–D214.
- 1918 Pacheco, A.R., Moel, M., and Segrè, D. (2019). Costless metabolic secretions as
1919 drivers of interspecies interactions in microbial ecosystems. *Nat. Commun.* 10, 103.

- 1920 Paik, D., Yao, L., Zhang, Y., Bae, S., D'Agostino, G.D., Zhang, M., Kim, E., Franzosa,
1921 E.A., Avila-Pacheco, J., Bisanz, J.E., et al. (2022). Human gut bacteria produce TH17-
1922 modulating bile acid metabolites. *Nature* 603, 907–912.
- 1923 Pascal Andreu, V., Roel-Touris, J., Dodd, D., Fischbach, M.A., and Medema, M.H.
1924 (2021). The gutSMASH web server: automated identification of primary metabolic gene
1925 clusters from the gut microbiota. *Nucleic Acids Res.* gkab353.
- 1926 Percy, M.G., and Gründling, A. (2014). Lipoteichoic acid synthesis and function in gram-
1927 positive bacteria. *Annu. Rev. Microbiol.* 68, 81–100.
- 1928 Piletz, J.E., Aricioglu, F., Cheng, J.-T., Fairbanks, C.A., Gilad, V.H., Haenisch, B.,
1929 Halaris, A., Hong, S., Lee, J.E., Li, J., et al. (2013). Agmatine: clinical applications after
1930 100 years in translation. *Drug Discov. Today* 18, 880–893.
- 1931 Price, M.N., Deutschbauer, A.M., and Arkin, A.P. (2022). Filling gaps in bacterial
1932 catabolic pathways with computation and high-throughput genetics. *PLoS Genet.* 18,
1933 e1010156.
- 1934 Pruss, K.M., Enam, F., Battaglioli, E., DeFeo, M., Diaz, O.R., Higginbottom, S.K.,
1935 Fischer, C.R., Hryckowian, A.J., Van Treuren, W., Dodd, D., et al. (2022). Oxidative
1936 ornithine metabolism supports non-inflammatory *C. difficile* colonization. *Nat Metab* 4,
1937 19–28.
- 1938 Ravcheev, D.A., and Thiele, I. (2014). Systematic genomic analysis reveals the
1939 complementary aerobic and anaerobic respiration capacities of the human gut
1940 microbiota. *Front. Microbiol.* 5. <https://doi.org/10.3389/fmicb.2014.00674>.
- 1941 Roager, H.M., and Licht, T.R. (2018). Microbial tryptophan catabolites in health and
1942 disease. *Nat. Commun.* 9, 3294.
- 1943 Rodionov, D.A., Arzamasov, A.A., Khoroshkin, M.S., Iablokov, S.N., Leyn, S.A.,
1944 Peterson, S.N., Novichkov, P.S., and Osterman, A.L. (2019). Micronutrient
1945 Requirements and Sharing Capabilities of the Human Gut Microbiome. *Front. Microbiol.*
1946 10, 1316.
- 1947 Schymanski, E.L., Jeon, J., Gulde, R., Fenner, K., Ruff, M., Singer, H.P., and Hollender,
1948 J. (2014). Identifying small molecules via high resolution mass spectrometry:
1949 communicating confidence. *Environ. Sci. Technol.* 48, 2097–2098.
- 1950 Seemann, T. (2014). Prokka: rapid prokaryotic genome annotation. *Bioinformatics* 30,
1951 2068–2069.
- 1952 Smith, N.W., Shorten, P.R., Altermann, E., Roy, N.C., and McNabb, W.C. (2020).
1953 Mathematical modelling supports the existence of a threshold hydrogen concentration
1954 and media-dependent yields in the growth of a reductive acetogen. *Bioprocess Biosyst.*
1955 *Eng.* 43, 885–894.

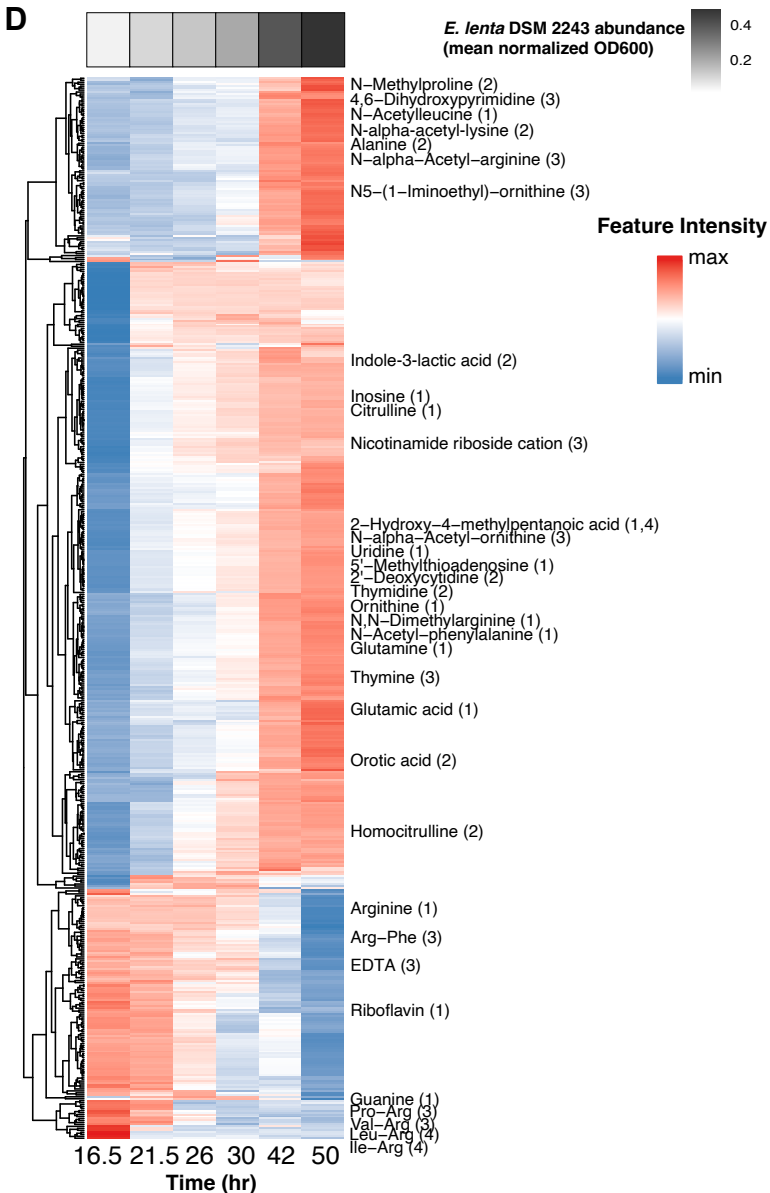
- 1956 Soto-Perez, P., Bisanz, J.E., Berry, J.D., Lam, K.N., Bondy-Denomy, J., and
1957 Turnbaugh, P.J. (2019). CRISPR-Cas System of a Prevalent Human Gut Bacterium
1958 Reveals Hyper-targeting against Phages in a Human Virome Catalog. *Cell Host Microbe*
1959 *26*, 325–335.e5.
- 1960 Sperry, J.F., and Wilkins, T.D. (1976). Arginine, a growth-limiting factor for *Eubacterium*
1961 *lentum*. *J. Bacteriol.* *127*, 780–784.
- 1962 Sprouffske, K., and Wagner, A. (2016). Growthcurver: an R package for obtaining
1963 interpretable metrics from microbial growth curves. *BMC Bioinformatics* *17*, 172.
- 1964 Strobel, H.J. (2009). Basic laboratory culture methods for anaerobic bacteria. *Methods*
1965 *Mol. Biol.* *581*, 247–261.
- 1966 Szöcs, E., Stirling, T., Scott, E.R., Scharmüller, A., and Schäfer, R.B. (2020). webchem
1967 : An R Package to Retrieve Chemical Information from the Web. *J. Stat. Softw.* *93*.
1968 <https://doi.org/10.18637/jss.v093.i13>.
- 1969 Thiele, I., and Palsson, B.Ø. (2010). A protocol for generating a high-quality genome-
1970 scale metabolic reconstruction. *Nat. Protoc.* *5*, 93–121.
- 1971 Tramontano, M., Andrejev, S., Pruteanu, M., Klünemann, M., Kuhn, M., Galardini, M.,
1972 Jouhten, P., Zelezniak, A., Zeller, G., Bork, P., et al. (2018). Nutritional preferences of
1973 human gut bacteria reveal their metabolic idiosyncrasies. *Nature Microbiology*
1974 <https://doi.org/10.1038/s41564-018-0123-9>.
- 1975 Venturelli, O.S., Carr, A.C., Fisher, G., Hsu, R.H., Lau, R., Bowen, B.P., Hromada, S.,
1976 Northen, T., and Arkin, A.P. (2018). Deciphering microbial interactions in synthetic
1977 human gut microbiome communities. *Mol. Syst. Biol.* *14*, e8157.
- 1978 Wang, M., Carver, J.J., Phelan, V.V., Sanchez, L.M., Garg, N., Peng, Y., Nguyen, D.D.,
1979 Watrous, J., Kapon, C.A., Luzzatto-Knaan, T., et al. (2016). Sharing and community
1980 curation of mass spectrometry data with Global Natural Products Social Molecular
1981 Networking. *Nat. Biotechnol.* *34*, 828–837.
- 1982 Weidenmaier, C., and Peschel, A. (2008). Teichoic acids and related cell-wall
1983 glycopolymers in Gram-positive physiology and host interactions. *Nat. Rev. Microbiol.* *6*,
1984 276–287.
- 1985 Wickham, H. (2016). *ggplot2: Elegant Graphics for Data Analysis*.
- 1986 Wohlgemuth, G., Haldiya, P.K., Willighagen, E., Kind, T., and Fiehn, O. (2010). The
1987 Chemical Translation Service--a web-based tool to improve standardization of
1988 metabolomic reports. *Bioinformatics* *26*, 2647–2648.
- 1989 Wolfer, A. (2022). Short Asynchronous Time-Series Analysis [R package santaR
1990 version 1.2.3].

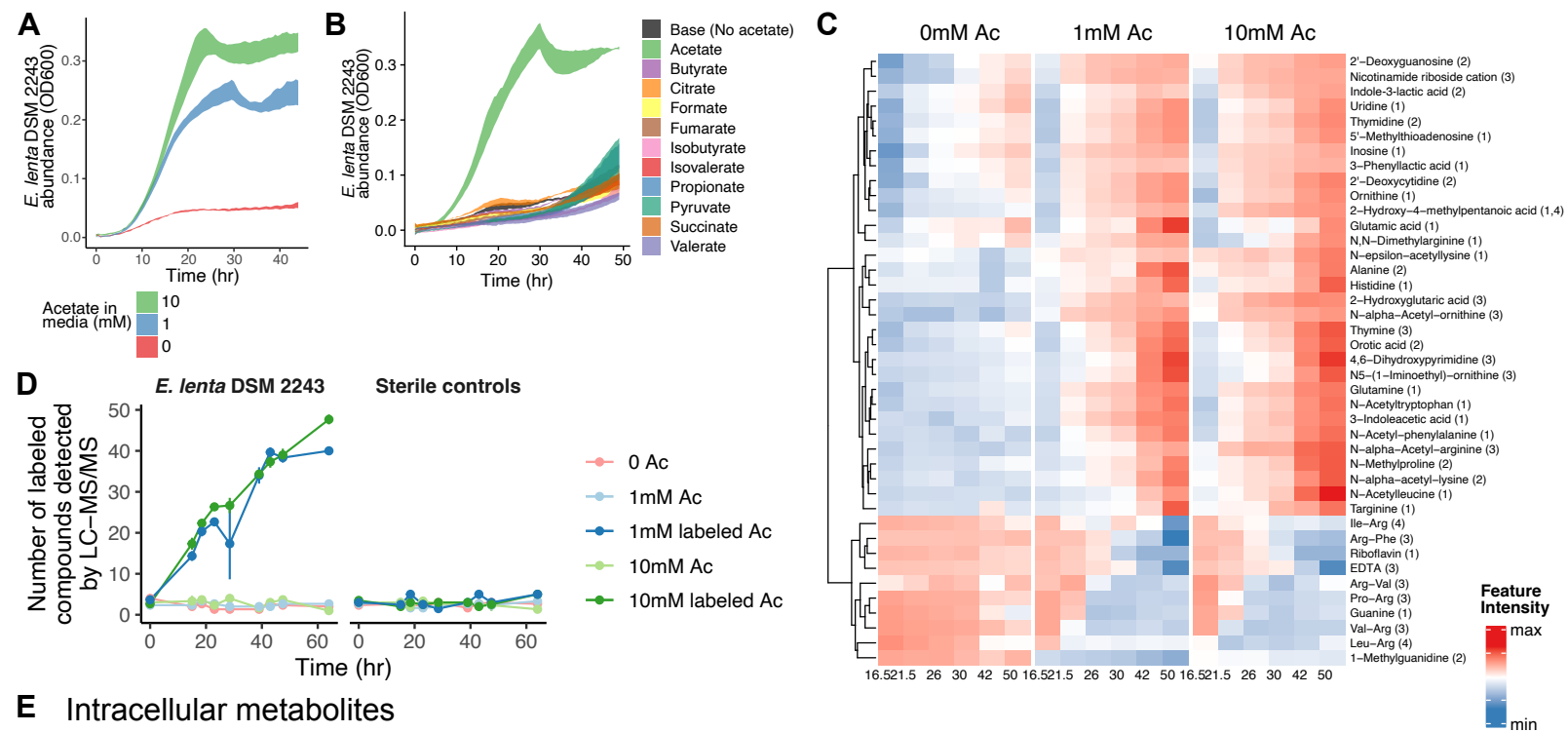
- 1991 Wu, T., Hu, E., Xu, S., Chen, M., Guo, P., Dai, Z., Feng, T., Zhou, L., Tang, W., Zhan,
1992 L., et al. (2021). clusterProfiler 4.0: A universal enrichment tool for interpreting omics
1993 data. *Innovation (Camb)* 2, 100141.
- 1994 Zhang, G., Mills, D.A., and Block, D.E. (2009). Development of Chemically Defined
1995 Media Supporting High-Cell-Density Growth of Lactococci, Enterococci, and
1996 Streptococci. *Appl. Environ. Microbiol.* 75, 1080–1087.
- 1997 Zhang, Y., Cai, J., Shang, X., Wang, B., Liu, S., Chai, X., Tan, T., Zhang, Y., and Wen,
1998 T. (2017). A new genome-scale metabolic model of *Corynebacterium glutamicum* and
1999 its application. *Biotechnol. Biofuels* 10, 169.
- 2000 Zhu, Q., Hou, Q., Huang, S., Ou, Q., Huo, D., Vázquez-Baeza, Y., Cen, C., Cantu, V.,
2001 Estaki, M., Chang, H., et al. (2021). Compositional and genetic alterations in Graves'
2002 disease gut microbiome reveal specific diagnostic biomarkers. *ISME J.*
2003 <https://doi.org/10.1038/s41396-021-01016-7>.
- 2004



Chemical Superclass

- Alkaloids and derivatives
- Nucleosides, nucleotides, and analogues
- Organic acids and derivatives
- Organoheterocyclic compounds
- Other





E Intracellular metabolites

